NTNU
Norwegian University of
Science and Technology

Mitigation of Uncertainties in Rainfall-Induced Landslide Prediction Models in a Changing Climate

Kvam Case Study

Liv Malin Ellen Mo Østgren

Civil and Environmental Engineering
Submission date: December 2017
Supervisor: Gudmund Reidar Eiksund, IBM
Co-supervisor: Ivan Depina, Sintef

Norwegian University of Science and Technology
Department of Civil and Environmental Engineering

NTNU

Fall 2017

Norwegian University of Science and Technology
Department of Civil and Environmental Engineering

MSc Thesis

TBA4900 – Geotechnical Engineering

Fall 2017
Liv Malin Ellen Mo Østgren

Mitigation of uncertainties in rainfall-induced landslide prediction models in a changing climate: Kvam case study.

BACKGROUND

Flooding and landslides are, next to storms, the most damage causing and deadly natural hazards in Norway. One of the main challenges in providing consistent and accurate predictions of rainfall-induced landslide occurrences is the large uncertainty involved in the analysis. Currently, there is a need to develop innovative and cost-efficient methods to obtain information on the uncertain geotechnical and environmental conditions controlling the occurrence of these landslides. The topic of this thesis is an alternative approach in reducing uncertainties by learning from observations of slope performances.

The topic was originally proposed by co-supervisor Ivan Depina at SINTEF, Trondheim, as a contribution to the Klima 2050 project. Klima 2050 - Risk reduction through climate adaptation of buildings and infrastructure is a Centre for Research-based Innovation (SFI) financed by the Research Council of Norway and the consortium partners.

TASK

The aim of the present Master Degree Thesis is to examine the potential of applying the Bayesian updating framework in reducing uncertainties associated with rainfall-induced landslides. A landslide event that occurred in 2011 in the Kvam area, Gudbrandsdalen is considered. The work includes the following sub-tasks:

1. Review of literature on the topic of rainfall-induced landslides, and characterization of the Kvam site and 2011 landslide event based on available literature.
2. Establishment of an analytical and a numerical probabilistic rainfall-induced landslide prediction model, with implementation of the Bayesian updating framework. Evaluation of the effect of model complexity on the updating process.
3. Evaluation of the effect of Bayesian updating on predicted slope factors of safety and on uncertain parameters of the prediction models. Evaluation of the effect of Bayesian updating on rainfall-induced landslide occurrence probabilities under climate change, by simulation of varying rainfall intensities and rainfall return periods.

NTNU fall 2017

Gudmund Eiksund

Supervisor:
Gudmund Eiksund (NTNU)

Ivan Depina

Co-supervisor:
Ivan Depina (Sintef)

Preface

This master's thesis in geotechnical engineering is written as part of the MSc in Civil and Environmental Engineering at the Norwegian University of Science and Technology (NTNU, Trondheim) during the fall of 2017. The original idea for this thesis was proposed by co-supervisor Ivan Depina at SINTEF, Trodnheim, as a contribution to the Klima 2050 project.

Klima 2050 - Risk reduction through climate adaptation of buildings and infrastructure is a Centre for Research-based Innovation (SFI) financed by the Research Council of Norway and the consortium partners. The aim of the project is to reduce the societal risks associated with climate changes, enhanced precipitation and flood water exposure within the built environment.

Oslo, December 20, 2017

Malin M Østgren

Liv Malin Ellen Mo Østgren

Acknowledgement

I would like to extend a special thank you to my co-supervisor Ivan Depina for his support and constructive feedback throughout the process. I am very grateful for his help with implementation of the analytical and numerical models used in this thesis and his valuable insights. The enthusiasm he has shown for the work has been inspiring.

Inputs from Gudmund Eiksund have also been well appreciated.

Abstract

One of the main challenges in providing consistent and accurate predictions of rainfall-induced landslides is the large uncertainty involved in the assessment. This thesis demonstrates the potential of an alternative approach in reducing uncertainties associated with rainfall-induced landslides by learning from observations of slope performances. The process is formalized by adopting the probabilistic Bayesian updating framework.

The performance of the implemented prediction models and the Bayesian updating framework is evaluated in a case study considering the landslide events that occurred in 2011 in the Kvam area of central Norway. Two types of landslide prediction models for slope stability under rainfall infiltration are implemented: simple analytical models and advanced sequentially coupled numerical models. Consistent trends between the models in terms of updated posterior probability density functions are observed.

The main contribution of this thesis is the implementation and demonstration of the updating framework in the described models. The results show that uncertainty in geotechnical and hydrological parameters controlling the occurrence of rainfall-induced landslides can be successfully reduced when the observation information in the updating process is constraining the outcome spaces of the random sample realizations. The parameters for which confidence intervals were reduced the most in the Kvam study were: soil thickness, groundwater table level, cohesion and friction angle. This indicates that these parameters are critical in the definitions of slope factors of safety in the implemented models. The effects of Bayesian updating on safety assessment of future rainfall-induced landslides is evaluated by simulating rainfall events of different return periods. The estimated probabilities of rainfall-induced landslide occurrence indicate that the strength of the updating information, in terms of constraining the random realization outcome spaces, and variation in rainfall return periods affects the estimated probabilities.

Sammendrag

En av hovedutfordringene ved kartlegging av flomskredfarer er de store usikkerhetene involvert i vurderingene. I denne masteroppgaven demonstreres en alternativ metode for å redusere usikkerhetene knyttet til flomskredskartlegging kalt Bayesisk oppdatering. Hovedprinsippet er å oppdatere sannsynlighetsfordelingene til de usikre geotekniske og hydrologiske parameterne med observasjoner av skredutsatte skråninger.

To typer modeller for å forutsi flomskredfare er implementert i arbeidet med denne oppgaven: enkle analytiske modeller og avanserte numeriske modeller. I oppgaven er en skredhendelse fra 2011 i områdene rundt Kvam, Gudbrandsdalen, brukt som bakgrunn for å evaluere de implementerte skred-modellene og oppdaterings-rammeverket. Resultatene, presentert i form av de oppdaterte annsynlighetsfordelingene til de usikre parameterne, indikerer konsekvente trender mellom de enkle og de avanserte modellene.

Resultatene viser at usikkerheten i geotekniske og hydrologiske parametere knyttet til utløsning av regnutløste flomskred kan reduseres ved hjelp av Bayesisk oppdatering når observasjonen som introduseres i modellen er definert slik at den begrenser utfallsrommet til de stokastisk modellerte parameterne. I Kvam-studien var skråningstykkelse, grunnvannstand, kohesjon og friksjonsvinkel de mest kritiske variablene i stabilitetsberegningene. Konfidensintervallene til disse parameterne ble redusert mest.

Effektene av Bayesisk oppdatering i sikkerhetsvurdering av fremtidige regnutløste flomskred ble vurdert ved å simulere nedbørshendelser med varierende intensitet og returperioder. Resultatene tilsier at styrken på oppdateringsinformasjonen; hvor begrensende den er på utfallsrommene, og variasjon i nedbørsperioder påvirker de estimerte sannsynlighetene for regnutløste flomskred.

Contents

List of Tables

List of Figures

List of Symbols and Abbreviations

Abbreviations

Acronym	**Description**
DEM	Digital elevation model
GW	Groundwater
MAMSL	Meters above measured sea level
MCMC	Markov Chain Monte Carlo
MCS	Monte Carlo Simulation
MET	Norwegian Meteorological Institute
NGI	Norwegian Geotechnical Institute
NGU	Geological Survey of Norway
NVE	Norwegian Water Resources and Energy Directorate
PDF	Probability density function
SWCC	Soil water characteristic curve
TRIGRS	A Fortran Program for Transient Rainfall Infiltration and Grid-Based Regional Slope-Stability Analysis
USGS	U.S. Geological Survey

Greek symbols

Symbol	**Description**	**Units**
Θ	Volumetric water content	-
Θ_r	Residual volumetric water content	-
Θ_s	Saturated volumetric water content	-
Ω	Sample space	-
α	Grain size ratio	-

Symbol	**Description**	**Units**
γ_s	Total unit weight of soil	kN/m^3
γ_w	Unit weight of water	kN/m^3
θ	Slope angle	$^\circ$
$\bar{\mu}$	Mean estimate	-
ρ_w	Density of water	g/cm^3
σ	Normal stress	kPa
σ'	Effective normal stress	kPa
$\bar{\sigma}$	Standard deviation estimate	-
τ	Shear stress	kPa
ϕ'	Effective internal friction angle	$^\circ$
ϕ_b	Angle indicating the rate of increase in shear strength with respect to a change in matric suction	$^\circ$
χ	Bishop's matric suction coefficient	-
ε	Modelling error	-

Roman symbols

Symbol	**Description**	**Units**
c'	Effective cohesion	kPa
D	Hydraulic diffusivity	m/s
D_0	Maximum hydraulic diffusivity	m/s
e	Void ratio	-
F_s	Factor of safety	-
g	Gravitational constant	m/s^2
g_a	Curve fitting parameter of Van Genuchten model	-
g_n	Curve fitting parameter of Van Genuchten model	-
g_c	Curve fitting parameter of Van Genuchten model	-
g_l	Curve fitting parameter of Van Genuchten model	-
H	Soil thickness (slope height)	m

Symbol	**Description**	**Units**
H_w	GW-table depth	m
h	Hydraulic head	m
h_p	Pressure head	m
$h_{p,0}$	Long term pressure head component of Iverson model	m
$h_{p,1}$	Short term pressure head component of Iverson model	m
I_z	Rainfall intensity	m/s
i	Hydraulic gradient	-
K_0	Coefficient of earth pressure at rest for total stresses	-
k	Permeability	m/s
k_{rel}	Relative permeability	-
k_{sat}	Saturated permeability	m/s
L	Slope lenght	m
n	Porosity	-
P_f	Probability of failure	-
p_0	Conditional probability of subset simulation process	-
q	Water flow rate	m/s
R	Response function of Iversons model	-
R_{peak}	Peak value of Iversons response function	-
S	Saturation ratio	-
S_r	Residual saturation	-
S_e	Effective saturation	-
T	Rainfall duration	day
T^*	Normalized rainfall duration	-
t^*	Normalized time	-
u_a	Atmospheric air pressure	kPa
u_w	Pore water pressure	kPa
v	Velocity of water	kPa
Z	Vertical coordinate of Iversons model	m

Chapter 1

Introduction

1.1 Motivation

Flooding and landslides are, next to storms, the most damage causing and deadly natural hazards in Norway (St.meld.15 (2012)). Landslides often occur simultaneously with extreme precipitation and snow melting (Sandersen et al. (1996)), and researchers generally agree that raised frequency of geohazards can be expected in the future in Norway as a consequence of climate change (NGI (2013), NGU (2009), Jaedicke (2009)). Norwegian authorities have a significant focus on climate change and safety preparedness for climate change-related problems like geohazards and landslides. This is evident trough the report from the Ministry of Petroleum and Energy ”How to live with the dangers - flood and landslides” (St. Meld. 15 (2012)), and the report ”Climate change adaptation in Norway” (St. Meld. 33 (2013)) from the Ministry of the Environment. Many public and privately funded projects have also been initiated in Norway concerning these topics, for instance GeoExtreme (duration 2005–2008), InfraRisk (2010-2013) and the ongoing Klima2050.

One of the main challenges in providing consistent and accurate predictions of the occurrence of rainfall-induced landslides, on both local and regional scales, is the large uncertainty involved in the analysis (Melchiorre and Frattini (2012), Zhang et al. (2011)). This includes uncertainties in geotechnical, hydrological and climate model paramaters due to lack of knowlegde (e.g., insufficient geotechnical investigations) and due to the inherent natural variability of the conditions in the field. The inability of models to correctly describe the complex physical behaviour of rainwater infiltration and landslide triggering mechanisms further adds to the uncertainty in predictions. Collecting information on the uncertain parameters is often a challenging task when the assessment areas are remote, heterogeneous and spanning tens of kilometers. Currently, there is a lack of reliable and cost efficient ways of obtaining information on the uncertainties controlling the occurrence rainfall-induced landslides (Depina (2017)).

Problem formulation

This thesis will focus on implementation of a method for handling uncertainties and reducing uncertainties in rainfall-induced landslide predictions based on information of observed slope performance. This will be formalized by adopting the Bayesian updating framework. The problem formulation is as follows: *How does information of slope performance affect the uncertainties involved in rainfall-induced landslide prediction?*

Literature survey

The main findings in the literature survey of this thesis can be divided into three parts.

First, numerous conceptual and physically based analytical and numerical models have been proposed to investigate slope stability under rainfall conditions. The comprehensive review on existing research on rainfall-induced landslides by Zhang et al. (2011) presents methods commonly applied in analyses. A crucial part of analyses is to solve the complex problem of infiltration of rainwater into the slope (Zhang et al. (2016), Fredlund (2012)). Solutions of second-order partial differential equations for water flow in saturated and unsaturated soil (e.g. Richards (1931)) are considered robust (Zhang et al. (2016)). Iversons simplified analytical solution (2000) has gained popularity because of its easy application and low computational demands. Numerical methods, on the other hand, are computationally demanding but can consider complex geometries and heterogeneity, and incorporate advanced models of unsaturated soil behaviour (e.g. Van Genuchten (1980)) (Plaxis (2016b)). In evaluation of slope stability, the extended Mohr-Coulomb failure criterion (Fredlund et al. (1978)) is usually adapted in both analytical limit equilibrium methods (Rahardjo and Leong (2007), Cho and Lee (2002)) and numerical studies (Plaxis (2016a)).

Second, in recent years, several probabilistic approaches to the problem of rainfall induced landslides has been examined in order to systematically and quantitatively account for the large amount of uncertainty involved. The book *Rainfall-Induced Soil Slope Failure* by Zhang et al. (2016) provides a good overview of rainfall-induced landslides from a probabilistic perspective, including many interesting case studies. Melchiorre and Frattini (2012) used a Monte Carlo approach (e.g. Baecher and Christian (2003)) to model probability of rainfall-induced shallow landslides under changing climate conditions in Otta, Central Norway. They found that accurate quantification of changes in stability conditions was not feasible, since the uncertainty in slope hydrological and in slope stability conditions was higher than in climatic change. Mitigation of uncertainties in probabilistic analyses can increase the robustness of landslide predictions (Depina (2017)). The Bayesian updating framework is advantageous because it provides an explicit and consistent approach to model uncertainties and update them with observations (Straub and Papaioannou (2015)). The framework has been successfully applied in back-calculation of landslide controlling parameters (Ering and Babu (2016), Zhang et al. (2010), Luo et al. (2017)).

Third, Chapter 3 in this thesis is a result of a literature survey on the Kvam area and the 2011 landslide event. In lack of available geotechnical field measurements, the site characterization is based on various sources of literature. This provides the background for the selection of uncertain geotechnical, hydrological and climate parameters in the case study.

What remains to be done?

Bayesian updating is a relatively new method in reliability engineering (Straub and Papaioannou (2015)). Few studies have examined the potential of using information of slope performance to learn about and reduce uncertainties in landslide prediction models (Depina (2017)). A key motivation for using observations of slope performance in the Bayesian updating framework originates from the low cost that is required to gather such information in comparison to more conventional methods for collecting data on uncertain geotechnical parameters.

1.2 Objectives

The investigation of the Bayesian updating method will be done trough a case study based on a landslide event in Kvam, Gudbrandsdalen, Norway in 2011, which is a case study site in the ongoing Klima2050 project. The main objectives are:

1. Establish tools for predicting rainfall-induced landslides.
2. Implement a probabilistic model to describe the uncertainties associated with the assessment of rainfall induced landslides.
3. Implement Bayesian updating to mitigate involved uncertainties.

4. Evaluate the effect of Bayesian updating on predicted slope factors of safety and on uncertain parameters of the prediction models.

5. Evaluate the effect of Bayesian updating on rainfall-induced landslide occurrence probabilities under climate change.

1.3 Limitations

The implementation of the Bayesian updating will be limited to updating prior model parameter distributions with the information of slope survival before and after the Kvam 2011 rainfall event.

The thesis will rely heavily on the analytical models. Due to time constraints and the high computational demands of doing probabilistic analyses with the numerical tools, only a limited number of numerical simulations are run. The effects of climate change on rainfall-induced landslide predictions are only evaluated for the analytical model.

1.4 Methods

The approach for objective 1 is to select two types of prediction models for rainfall-induced landslides: analytical and numerical models. The chosen analytical models will be calculated with a code in Phyton. The numerical rainfall infiltration and slope stability models will be implemented in Plaxis 2D, and a sequential coupling of these is done with a Phyton code.

Objectives 2 and 3 will be carried out by formulating reliability models with Bayesian updating in Phyton code, using direct Monte Carlo and Subset simulation techniques. The selection of model parameters and the definition of the updating information will be based on the literature study for the Kvam area. Comparison of prior and posterior distributions and mean and 95% confidence estimates of factors of safety and parameter values will be done to evaluate the effects of updating on uncertainties. Data processing will be done in Python.

The approach for Objective 5 is to perform a simple probabilistic analysis of slope stability under infiltration of rainfall with different intensities and return periods, corresponding to present and future climate scenarios.

1.5 Thesis outline

The remaining part of the thesis is structured in four chapters. Chapter 2 presents the implemented analytical and numerical rainfall models for rainfall infiltration and slope stability prediction. A basic overview of groundwater flow and slope stability theory is given as well. Chapter 3 provides the basic elements of the implemented probabilistic methods, including the Bayesian updating framework. In Chapter 4 the Kvam case study is presented, with specification of the model uncertainties, the updating process and the updating information. Results of the case study are presented with discussions at the end of the chapter. A summary with key findings as well as recommendations for further work is given in Chapter 5.

Chapter 2

Prediction tools

2.1 Rainfall-induced landslide characteristics

As an introduction to the descriptions of the implemented prediction tools and the theory behind these models, a brief characterization of rainfall-induced landslides is given.

A general characterization of landslide types observed in association with rainfall and flooding is given by Norwegian Water Resources and Energy Directorate (NVE) (2013): The slides triggered by rainfall and flooding are typically no more than 2 meters deep with high length to depth ratios, and can thus be characterized as shallow. Sliding surfaces are typically located within the soil cover and/or bedrock interface. Inland in Norway, rainfall-induced sliding most often occurs on valley sides in till deposits of fluvial, glacial and glacio-fluvial types. Observed slope angles commonly range between 20 and 45 °.

2.1.1 Mechanisms of rainfall-induced landslides

It is generally recognized that rainfall-induced landslides are caused by changes in pore water pressures and seepage forces (Collins and Znidarcic (2004)). Two main triggering scenarios that apply to heavy rainfall associated landsliding activity are mainly discussed (NVE (2013), Jaedicke et al. (2008)). One scenario is heavy surface erosion by short-term intense rainfall and flooding. In this case, erosion of deposits often happen along creeks or old derbis transport zones (NVE (2013)). The second scenario, which this thesis aims attention at, is initiation as a shallow landslide due to changes in pore water pressures. In this case the landslide masses may quickly develop into large derbis-flows due to high water contents and continued erosion along the failure path, but the initiating mechanism is different (NVE (2013)).

Collins and Znidarcic (2004) analyzed two distinct failure mechanisms of shallow rainfall-induced landslides due to pore pressure changes. In the first mechanism, typical for coarse grained soil, increased positive pressures due to saturation of the soil is observed in a low area on the slope or along the soil/bedrock interface. The decrease in effective stresses here result in failure and movement along the sliding surface. The stress path can be described as a constant shear stress path (Anderson and Sitar (1995)). In the second mechanism, typically observed in more fine grained soil, sliding is initiated in unsaturated soil. Slope failure is then due mainly to loss of shear strength when soil suctions are decreased or dissipated during rainfall infiltration (Fredlund (2012)). Ering and Babu (2016) argued that in hillsides consisting of various grain sizes, like till deposits, the two mechanisms cannot separately attribute to slope failure. Rather, combinations of mechanisms may cause failure.

Analyses of rainfall-induced landslides are commonly divided into two stages (Cascini et al. (2010)): The first stage, initiation, can be defined as the formation of a continuous failure surface. The second, post-failure stages, can be characterized by generation of large plastic strains and acceleration of the failed soil mass. These two stages are often analyzed separately due to significant differences in the behavior of the soil masses in the two stages. The focus of this thesis is the first stage; slope failure and triggering mechanisms.

2.1.2 Factors controlling rainfall-induced landslides

Rainfall-induced landslides are complex in nature. The review of existing research on infiltration and slope stability analysis under rainfall infiltration by Zhang et al. (2011) provides a concise summary of studies on factors controlling occurrence of failure. Generally, soil shear strength properties, slope angles, soil thickness and the groundwater conditions (e.g. pore pressure and suction distribution) determines the initial stability situation before rainfall (Rahardjo and Leong (2007)). The actual failure conditions are much determined by rainfall characteristics and the response to rainfall, governed by soil hydraulic properties (Zhang et al. (2011)).

The groundwater conditions and flow patterns in till slopes can vary significantly with time. During dry periods, up slope groundwater tables (GW-tables) in till are usually low, and water movement is mainly vertically downward during rainfall or even occasionally reversed by evaporation and transpiration (Lars Lundin (1990a)). During wet periods however, which is usually the initial condition of rainfall-induced slope failure in springtime (Jaedicke et al. (2008), Walberg and Devoli (2014), NVE (2013), Edvardsen (2013)), the soil may be saturated throughout the whole profile due to heavy snow melting combined with rainfall. Under these conditions, especially in sandy and sandy-silty till, slope-parallel water flow may occur, even above the water table (Lars Lundin (1990a)). During long and/or intense rainfalls, the till deposits up slope can become fully saturated or the infiltration capacity can be exceeded. This can again result in locally large runoff and erosion rates (Walberg and Devoli (2014)).

Significant spatial variation of initial groundwater situations and rainfall responses is also typical within basins and even single slopes (Lars Lundin (1990a), Lars Lundin (1990b)). The shape of the basin and slope is a major determinant of water flow patterns, as slides usually form in old landslide scars, ravines, along creeks and rivers or in convex basins with enough water inflow (NVE (2013), Heyerdahl (2016), (Lars Lundin (1990a)). Moreover, human intervention in the basin can alter the flow patterns (NVE (2013)). Roads and railroads can drain and redistribute surface water flow. Tree-felled areas can also be vulnerable to landsliding activity because of reduced evapotranspiration and increased water storage capacity in macropores replacing rotten roots (Lars Lundin (1990a)).

2.2 Rainfall-infiltration models

2.2.1 Basic theory of water flow in soil

In the following, some key concepts of saturated and unsaturated water flow are summarized to provide a background for the rainfall infiltration analyses done in this thesis. The theory presented is adapted from the book *Unsaturated Soil Mechanics in Engineering Practice* by Fredlund (2012) unless other references are given.

The driving potential for water flow is hydraulic head, a measure of the energy level of the water in a given point. An expression for the total hydraulic head h at a depth z relative to some reference is:

$$h = z + \frac{u_w}{\rho_w g} + \frac{v^2}{2g} \tag{2.1}$$

Here, u_w, ρ_w, g, and v is the pore water pressure, the water density, the gravitational acceleration constant and the velocity of the water, respectively. z is known as the gravitational head (vertical coordinate with positive direction upward), $\frac{u_w}{\rho_w g}$ is the pressure head h_p and $\frac{v^2}{2g}$ is the velocity head. Velocity head is usually negligible because of the low flow velocities in soil.

A difference in potential over a length in space, will cause water to flow. This is described by Darcy's law 1856:

$$q = -k\frac{\partial h}{\partial l} = -ki. \tag{2.2}$$

where q is the water flow rate, i is the gradient of hydraulic head, and k is the coefficient of permeability of the soil, given in units of length/time. The negative sign is used because water flows from a higher to lower potential, meaning that a negative head change will happen over a positive ∂l. When the flow rate in a soil is equal to the permeability, the hydraulic gradient $i = -q/k = -1$. This corresponds to a steady-state flow, and the hydraulic head and the coefficient of permeability are constant. A situation where there is no flow in the soil, $i = 0$, is called hydrostatic. When considering problems of rainfall infiltration into soil, it is often of interest to analyze how suction and pore pressures change time-dependently during infiltration. One is then looking at a transient situation, often a transitional state between an initial and end steady state situations. In a transient flow analysis, the hydraulic head and the coefficient of permeability are not constant.

In unsaturated soils, both water and air are classified as fluids that can flow. In this thesis, pore-air pressures is assumed to remain atmospheric, u_a, and taken as the zero pressure reference level. The matric suction, $u_a - u_w$, in the soil will be equal to $-u_w$.

2.2.2 Unsaturated soil characteristics

The response of unsaturated soil to water infiltration depends on the unsaturated hydraulic properties of the soil. Permeability, the proportionality factor of Darcy's law, controls how easily water can flow through the pores of the soil. Saturated permeability, k_{sat}, is the permeability of the soil when all pores are filled with water. The value of permeability of a soil depends on porosity, distribution of pores and fractures as well as homogeneity and isotropy (Lars Lundin (1990b)). These are properties controlled mainly by grain-size distribution, structural properties, particle spatial distribution and orientation and degree of soil compaction (Haldorsen and Krüger (1990)).

In unsaturated soils, k varies mainly with changes in the stress state of the soil and the degree of saturation, S. The number of fluid-connected pores and channels available for the flow of water in a soil decrease with decreasing water content, and consequently the permeability is lowered. The reduction of k with decreasing S is rapid and usually occurs over several orders of magnitude. This rapid decrease can be explained by the desaturation process, in which the biggest pores dries first. As the soil dries, water is forced to move trough smaller and smaller pores, resulting in increasing turtuosity of flow and significantly decreasing flow rates.

Relationships relating permeability, saturation and hydraulic head are needed in order to correctly describe unsaturated soil responses to rainfall infiltration. The relationship relating S to matric suction or hydraulic head is commonly described by a Soil Water Characteristic Curve (SWCC). A complementary permeability function can describe how the coefficient permeability, or relative permeability $k_{rel} = k/k_{sat}$, varies with suction. These relationships can be directly determined in the field or by using laboratory methods. However, since measurement of these relationships is challenging and often time consuming, many empirical models have been proposed.

One popular model is the one proposed by Van Genuchten (1980): a SWCC equation with three input parameters: saturated water content, θ_{sat}, and two curve fitting parameters. The three-parameter equation is formulated (Van Genuchten (1980)):

$$S = S_r + (1 - S_r)\left[1 + \left(g_a \frac{u_a - u_w}{\rho_w g}\right)^{g_n}\right]^{g_c}. \tag{2.3}$$

The complimentary permeability of the Van Genuchten model is defined:

$$k = k_{sat} S_e^{g_l}\left[1 - \left(1 - S_e^{(\frac{1}{g_c})}\right)^{g_c}\right]^2. \tag{2.4}$$

Here, $g_a, g_n, g_c = \frac{1-g_n}{g_n}$ and g_l are fitting parameters. g is gravitational acceleration. S_e and S_r is effective and residual degree of saturation, related trough the equation (Brooks (1964)):

$$S_e = \frac{S - S_r}{1 - S_r} \tag{2.5}$$

The curve fitting parameters can be determined based on information about the soil type. Characteristic values of the Van Genuchten model parameters for a range of soil types from Plaxis (Plaxis (2016a)) are presented below in the Table in Figure 2.1. As discussed by Vogel et al. (2000), the selection of curve fitting parameters can significantly affect the results of numerical simulations of transient flow, including the numerical stability and rate of convergence.

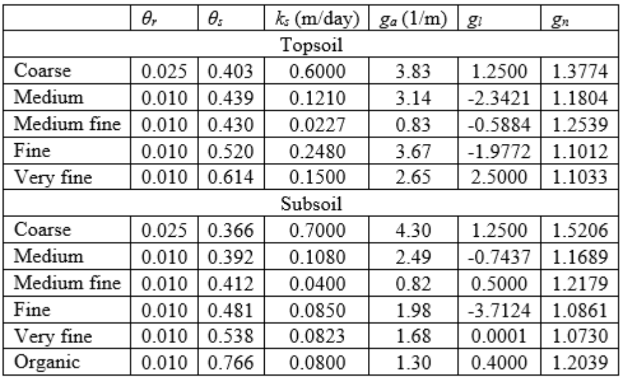

	θ_r	θ_s	k_s (m/day)	g_a (1/m)	g_l	g_n
Topsoil						
Coarse	0.025	0.403	0.6000	3.83	1.2500	1.3774
Medium	0.010	0.439	0.1210	3.14	-2.3421	1.1804
Medium fine	0.010	0.430	0.0227	0.83	-0.5884	1.2539
Fine	0.010	0.520	0.2480	3.67	-1.9772	1.1012
Very fine	0.010	0.614	0.1500	2.65	2.5000	1.1033
Subsoil						
Coarse	0.025	0.366	0.7000	4.30	1.2500	1.5206
Medium	0.010	0.392	0.1080	2.49	-0.7437	1.1689
Medium fine	0.010	0.412	0.0400	0.82	0.5000	1.2179
Fine	0.010	0.481	0.0850	1.98	-3.7124	1.0861
Very fine	0.010	0.538	0.0823	1.68	0.0001	1.0730
Organic	0.010	0.766	0.0800	1.30	0.4000	1.2039

Figure 2.1: *Characteristic values of Van Genuchten model parameters for various soil types (Plaxis (2016a)).* $\Theta_r = nS_r$ *and* $\Theta_s = nS_{=1}$ *are the residual and saturated volumetric water contents, respectively, with* n *= porosity.*

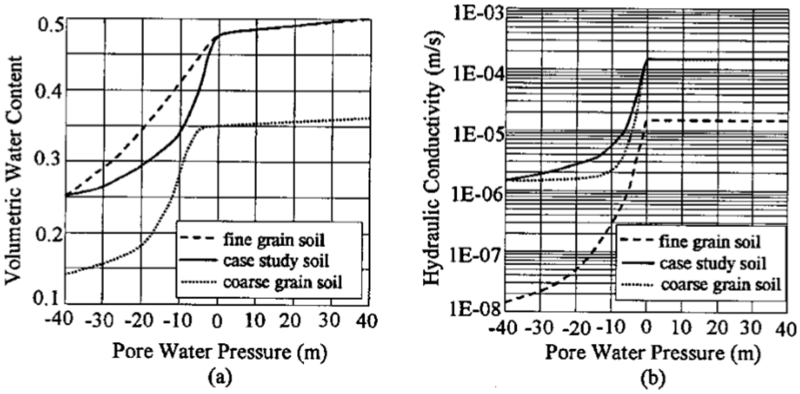

Figure 2.2: *Coarse grain soil and fine grain soil unsaturated characteristic curves: (a) SWCC and (b) suction-permeability curve (Credit: Collins and Znidarcic (2004)).*

Typical SWCC's and permeability-suction curves for a fine and a coarse grained soil are shown above in Figure 2.2 (Collins and Znidarcic (2004)). The curves describe several important characteristics of unsaturated soil. As discussed above, permeability reduces rapidly with desaturation and increased suction. Furthermore, Figure 2.2 (a) shows that above the water table, soils will not be fully unsaturated, but have considerable moisture contents. By examination of the volumetric water content reduction rates with pore pressure, it can be deduced that the transition from a unsaturated to saturated state under rainfall infiltration will be more gradual for a fine grained soil. With more pores initially filled with water in the unsaturated state, there are more pore channels available for water flow and thus resistance to flow is minimized. Still, the saturation process will go slower in this soil due to the low values of hydraulic conductivity visible in Figure 2.2 (b).

2.2.3 Governing equation of flow in saturated and unsaturated soil

A partial differential equation for transient and steady-state groundwater (GW) flow in unsaturated soils is presented in this section. A two-dimensional formulation is in focus due the common use of two-dimensional infiltration models for analysis of rainfall-induced landslides. According to mass conservation for water flow, total water outflow from a given volume is equal to the total change in mass concentration of water in the volume. Based on mass conservation and Equation (2.2), transient two-dimensional water flow in homogeneous, isotropic saturated-unsaturated soil can be modelled by the following equation (Richards (1931)):

$$\frac{\partial}{\partial x}\left[k(h_p)\frac{\partial h}{\partial x}\right]+\frac{\partial}{\partial y}\left[k(h_p)\frac{\partial h}{\partial y}\right]=-\frac{\partial \Theta(h_p)}{\partial t} \tag{2.6}$$

where h_p = is pressure head, and $\Theta = \rho_w n S$ is volumetric water content, with parameters n and S being the porosity and degree of saturation of the soil, respectively. For steady state conditions, the volumetric water content in the soil is constant with time, and the right side of (2.6) will be equal to 0.

Equation (2.6) is formulated uncoupled. That is, it is derived considering continuity of the water phase only. In order to analyze time dependent mechanical behaviour in partially saturated soils properly, mixed partial differential equations of soil displacement and pore pressure, must be solved simultaneously (Galavi (2010)) In this thesis, uncoupled formulations are chosen due to the focus on minimizing the numerical complexities and computational demands. More information on the implementation of coupled hydro-mechanical approaches in the finite element program Plaxis can be found in Galavi (2010).

Calculation of developing pore pressure and saturation profiles developing under rainfall infiltration and groundwater seepage with Richard's Equation, (2.6), is complicated because of the high non-linearity and complexity involved. (2.6) can be evaluated numerically, or analytically for given assumptions and approximations (Zhang et al. (2011)). In this thesis, two methods for analyzing time-dependent pore pressure development under rainfall-infiltration are implemented and

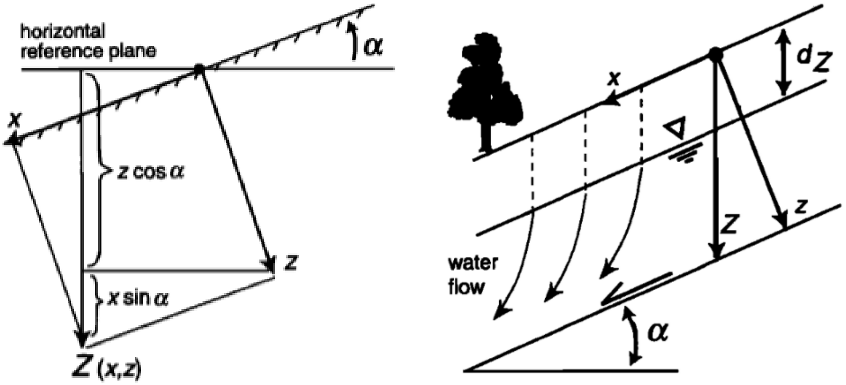

(a) (b)

Figure 2.3: *(a) Definition of the vertical coordinate* $Z = x \sin \theta + z \cos \theta$ *used to calculate elevation head or depth at an arbitrary location (x, y). Slope angle was denoted* α *in Iversons formulation (b) Illustration of Iversons model with rainwater infiltrating down the slope. The GW-table depth* $H_w = d_Z$ *(Figures: Iverson (2000)).*

compared: an analytical model and a numerical model. The two infiltration models are explained in the following sections.

2.2.4 Analytical infiltration model

Many analytical and quasi-analytical solutions to governing equations of unsaturated flow have been developed (Zhang et al. (2011)). The number and types of input parameters, complexities considered and assumptions made vary a lot between the methods. The many assumptions and simplifications limits the methods abilities to correctly describe all aspects of unsaturated flow in some situations (Zhang et al. (2011)). Nevertheless, analytical models are usually implemented in rainfall triggered landslide susceptibility analysis. As these analyses are often done at a regional scale and/or consider statistical distributions of input parameters, analytical methods are practical. The analytical infiltration model implemented in this thesis is a solution of Richard's equation presented by Iverson in 2000. Its low number of input parameters required and low computational demands, makes it a popular solution for the infiltration problem in rainfall triggered landslide analysis (Melchiorre and Frattini (2012), Zhang et al. (2011)). For instance, one of the most commonly used tools for transient rainfall infiltration and grid-based regional slope-stability analysis, USGS's program TRIGRS, is also based on Iverson's solutions (USGS (2008)). In the following paragraphs, the Iverson model is explained briefly.

Iverson (2000) presented an approximation of the governing equation (Equation (2.6)) that can describe groundwater pressures developing in slopes in response to rainfall over varying time periods. Starting out, a coordinate system is defined as shown in figure 2.3 (a). This means, that whenever the Iverson model is in focus, *Z has a positive direction downward.* Iversons model decomposes the time dependent pressure head distribution in a slope into two components. The first being the long term component, $h_{p,0}$, produced by a long-term infiltration rate and/or seepage pattern, and the second being the short term response to rainfall $h_{p,1}(t)$:

$$h_p(t) = h_{p,0} + h_{p,1}(t). \tag{2.7}$$

Iversons model is valid for different initial conditions; (1) a steady state pressure head distribution determined by a normalized steady state water table recharge rate, (2) hydrostatic or (3) slope-parallel steady state seepage (Iverson (2000)). In lack of available field measurements of groundwater levels, the initial conditions can be determined based on the topography and long term measurement rates, as shown in Melchiorre and Frattini (2012). In this thesis, the third initial situation (Ref. (2.11a)), is assumed for simplicity. Based on previously mentioned discussion of GW-flow in Lars Lundin (1990a), the assumption is reasonable.

The second short-term component of the pressure head response is is evaluated based on the reduced form of the Richards equation. Focusing on wet initial conditions and thereupon assuming $k_Z \approx k_{sat}$, the model does not consider unsaturated behaviour described by SWCC's and unsaturated permeability functions. With this assumption and further approximations, Equation (2.6) is reduced to the following diffusive form (Iverson (2000)):

$$\frac{\partial h_{p,1}}{\partial t} = D_0 \cos^2\theta \frac{\partial^2 h_{p,1}}{\partial Z^2} \tag{2.8}$$

(refer to Iverson (2000) for details). Here, θ is slope angle, $h_{p,1}$ is the time-dependent pressure head and D_0 is the maximum hydraulic diffusivity, a parameter determining the transmission of pressure head in the soil profile. It is defined as a function of k_{sat} and the rate of change in volumetric water content with pressure head. Solving (2.8) for appropriate initial and boundary conditions, the following set of equations can be used for calculation of ground water pressure at all depths Z and times t (Iverson (2000)):

$$\frac{h_p}{Z}(Z, t \leq T) = (1 - \frac{H_w}{Z})\cos^2\theta + \frac{I_z}{k_z}[R(t^*)] \tag{2.9a}$$

$$\frac{h_p}{Z}(Z, t > T) = (1 - \frac{H_w}{Z})\cos^2\theta + \frac{I_z}{k_z}[R(t^*) - R(t^* - T^*)] \tag{2.9b}$$

in which T is the duration of precipitation, $t_* = \frac{t}{Z^2/D}$ and $T_* = \frac{T}{Z^2/D}$ are the normalized time and normalized precipitation duration, respectively, D is a measure of effective hydraulic diffusivity equal to $4D_0\cos^2\theta$[1] and R is the response function

$$R(t^*) = \sqrt{t^*/\pi}e^{(-1/t^*)} - \text{erfc}(1/\sqrt{t^*}). \tag{2.10}$$

The solutions (2.9a) and (2.9b) obey the following initial and boundary conditions:

$$h_p(Z, 0) = (Z - H_w)\cos^2\theta \tag{2.11a}$$

$$\frac{\partial h_p}{\partial Z}(\infty, t) = \cos^2\theta \tag{2.11b}$$

$$\frac{\partial h_p}{\partial Z}(0, t) = \begin{cases} -I_z/k_z + \cos^2\theta & t \leq T, \\ \cos^2\theta & t > T, \end{cases} \tag{2.11c}$$

(2.11b) and (2.11c) implies that Darcy's law governs water entry at the ground surface, but at great depths, transient vertical seepage decays to zero and steady state pressures persist (Iverson (2000)). This is illustrated in Figure 2.3 (b).

$I_z = k_{sat}$ defines the maximum rainfall infiltration intensity in the model. The rainfall in excess of k_{sat} is assumed to run off the slope. In reality, ponding of water and build-up of positive pore pressures at the surface is possible (Fredlund (2012)).

Because of the constant flux boundary condition at the surface and lack of gravity drainage term in the linear diffusion model, Iverson's solution can provide physically unrealistic high pressures to develop at shallow depths. To avoid this, an ad-hoc solution implemented by Iverson (2000) was to limit the predicted pressures to a steady state condition $h_p = (Z - H_w)\cos^2\theta$.

---

[1] From here on, D_0 will be referred to as diffusivity, since this is the input parameter in the model

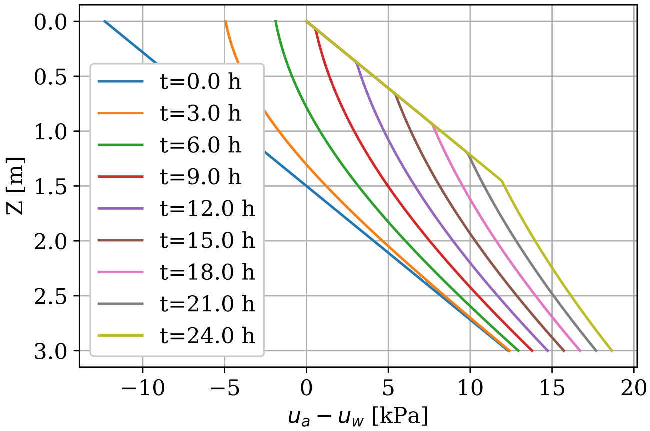

Figure 2.4: *Performance of the implemented analytical infiltration model with paramters* $k = k_{sat} = 1 \cdot 10^{-6}$*m/s and* $D_0 = 1 \cdot 10^{-4}$*: development of the predicted pore pressures with time*

However, Tsai and Yang (2006) showed that even with this correction, unrealistically high pressure heads can be estimated with Iverson's solution, due mainly to the overestimation of infiltration rate. They modified the ground surface boundary conditions and applied a finite-element method together with an iterative procedure to solve the problem.

Some other possible analytical solutions that were evaluated for implementation in this thesis should also be mentioned, just for information. (Conte and Troncone (2012)) presented an new alternative to Iverson's solution, also considering initially ”wet” slopes. For drier initial conditions, (Zhan et al. (2013)) presented a solution for infiltration in the unsaturated zone, taking the SWCC and permeability function into account. Another simple model is also presented in an alternative framework to TRIGRS (Montrasio (2000),Schilirò et al. (2016)).

It is of interest to examine the performance of Iversons model for Kvam case study relevant conditions. This can illustrate some of the consequences of the assumptions the model is built on. Figure 2.4 shows calculated pore pressure profiles for a 3 m high slope with $\theta = 25°$ and GW-table depth $H_w = 1.5$ m. A constant rainfall intensity $q = I_z = 60$ mm/day $= 6.9 \cdot 10^{-7}$ m/s is applied and studied for a 24 hours. The soil properties are defined as the mean values presented later in section 4.3 *Case study parameter estimates* on page 57. For the hydraulic properties, the following values are selected: $k = k_{sat} = 1 \cdot 10^{-6}$m/s and $D_0 = 1 \cdot 10^{-4}$ m/s.

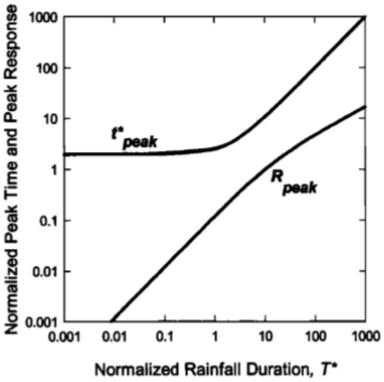

Figure 2.5: *Graphs of the peaking behavior of Iversons pressure head response function for a range of normalized rainfall durations. Graphs of the time to peak* t^*_{peak} *and magnitude of the peak response* R_{peak} *were constructed by evaluating* $R(t^*) - R(t^* - T^*)$ *for a range of* T^* *(Credit: Iverson (2000).*

Iverson's solutions do not take unsaturated behaviour models as those described in Section 2.2.2 into account, so the results in Figure 2.4 cannot be explained based on that theory. The pore pressures that develop instead depend on D_0 and the ratio I_z/k_z, in addition to the rainfall duration. In Iverson (2000), behaviour of the the response function is illustrated for a range of T^* values. Figure 2.5 shows that for low T^* values, the time to peak response, R_{peak}, given by t^*_{peak}, is nearly constant and $t^*_{peak} > T^*$. R_{peak} is also small for these values. This implies that if D_0 becomes too small in relation to t and T, rainfall infiltration has little effect on pore pressures in the slope. The unbounded growth of R_{peak} with T^* in Figure 2.5 also demonstrates how unrealistically high pressures would develop at the surface without the steady state correction (Iverson (2000)). For the chosen input values, $T^* \approx 3$, and influence of the rainfall on the pore pressures distribution can be observed (Ref. 2.4).

The initial situation at $t = 0$ h in Figure 2.4 is defined according to (2.11a). After infiltration starts, the negative suction reduces at the slope surface. After $t = 9$ h, the steady state condition is imposed at the surface. As more rainwater continues to infiltrate, steady state conditions are implied further down the soil profile. At the end of the rainfall, $t = 24$ h, pore pressures have increased by about 10 kPa above the GW-table, and slightly less below this level. It can also be observed here that the response function does not consider the GW-table level H_w when applying the steady state condition.

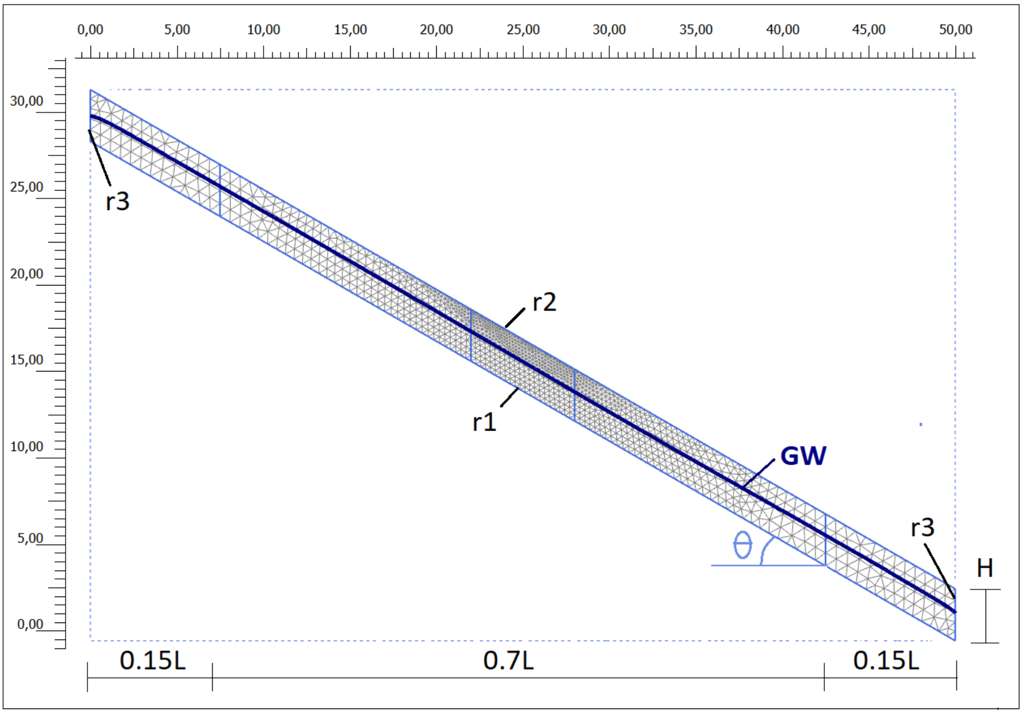

Figure 2.6: *Illustration of Plaxis model geometry and boundary conditions*

2.2.5 Numerical infiltration model

One way of overcoming some of the limitations of analytical solutions to governing flow equations, is to use numerical methods. The finite element program Plaxis 2D supports numerical evaluation of both coupled and uncoupled governing equations (Plaxis (2016c)). As discussed above, an uncoupled numerical flow and stability analysis in Plaxis is selected for this study. Analyses based on formulations of steady state and transient two-dimensional flow are performed, incorporating the Van Genuthcen model of unsaturated soil characteristics.

Figure 2.6 illustrates the geometry and boundary conditions of the implemented numerical model. The division of the slope into three sections is a measure made to prevent numerical instabilities, discussed in section 2.3.3. Increased mesh refinement is applied in middle section where results are studied. The bottom boundary, Γ1, defining the bedrock interface, is assumed impervious. It is defined as a closed boundary, meaning zero flow normal to the boundary. To the Γ3 boundaries, seepage boundary conditions are applied. Over these boundaries, water can flow in or out freely below and at the GW-level. An external total head given by the hydrostatic conditions is assigned at, and below, this level, and it may vary time-dependently. For the portions of the boundaries above the GW-line with unsaturated conditions, the boundaries are closed, and remains closed throughout the time-dependent parts of the analysis. Due to this, is important that the model-slope has a long lenght-to-height ratio. If pore pressures and other time-dependent GW-characteristics are measured in the middle of the slope, this prevents the prescribed closed parts of the end boundaries to affect the behaviour. The top boundary setting, $\Gamma 4$, changes between the stages of the analysis. (Plaxis (2016c)).

The rainfall infiltration analysis in this thesis is divided into two stages:

1. Steady state flow analysis, accounting for the long-term infiltration rates in the slope.
2. Transient flow analysis, determining the short-term raifall infiltration response.

In the first stage, the steady state pore pressures are determined based on the hydraulic conditions. Initial values of hydraulic head, permeabilities, degrees of saturation and suction levels in the unsaturated zone above the GW-level are determined by the unsaturated characteristics given by the Van Genuchten model. Simple hydrostatic suction profiles are considered. Evaporation is assumend negible preceeding the rainfall, which is reasonable under cloudy conditions. Influence of antecedent rainfall is neglected for the sake of simplicity. Below the GW-table, the soil is fully saturated, and pore pressures are determined by GW-table level. For this stage of the analysis, a seepage condition is assigned to the soil surface boundary $\Gamma 1$.

The second stage of the analysis is a time-dependent flow calculation. Here, pore pressures and GW-levels are again determined based on saturated and unsaturated hydraulic conditions. A rainfall is applied by assigning an infiltration boundary condition to the soil surface $\Gamma 1$. The rainfall can be modelled either as a constant inflow rate or a time-dependent inflow function. If the rate exceeds the soils capacity, ponding takes place at a default depht $h_{max} = 0.1$. This happens either if the soil is fully saturated or the infiltration rate exceeds k_{sat}.

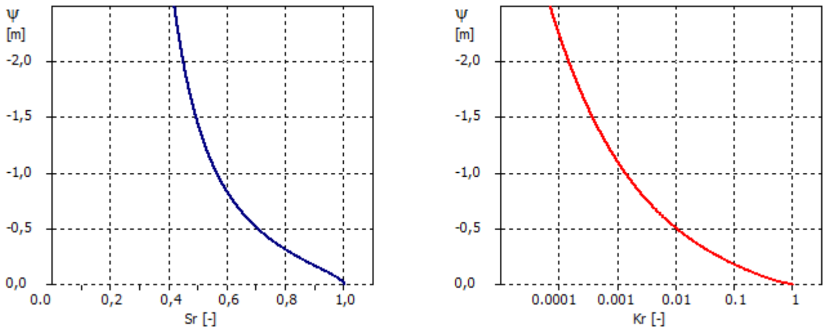

(a) **(b)**

Figure 2.7: *Graphs of the implemented Van Genucthen model: (a) coefficient of relative degree of saturation, (b) coefficient of relative permeability. Values on the y-axis defines pressure head levels.*

In the following, an example of the numerical model performance is presented. The slope geometry in this example is specified with $H = 3.0m$, $H_w = 1.5$ m and $\theta = 30°$. The inputs of the Van-Genuchten model are specified to $k_{sat} = 5 \cdot 10^{-6}$ m/s and a grain size distribution with: 19% particles $< 2\mu$m, 41% between 2μm and 50μm, and 40% between 50μm and 2 mm. The resulting Van-Genuchten graphs are shown in Figure 2.7. In the transient stage, a constant rainfall intensity of I_z =60 mm/day $= 6.9 \cdot 10^{-7}$ m/s is applied and studied for 24 hours.

The resulting development of the pore pressure with depth and time can be studied in Figure 2.8 on the next page. The pore pressure profiles are plotted with time intervals of 3 h over the vertical height of the soil. At $t = 0$ h, a hydrostatic situation is observed, corresponding to the input hydraulic properties. Above the prescribed GW-table depth of $Hw = 1.5$, lies a capillary zone of about 0.2 m, where degree of saturation ranges from 100% to 90%.

After $t = 0$ h, as the transient analysis with rainfall infiltration starts, the suction in the upper part of the unsaturated zone decreases (Ref. Figure 2.8). Since $I_z < k_{sat}$, suction decreases with t, but is not eliminated before the analysis termination at $t = 24$ h. Suction can only be eliminated fully if the rainfall intensity is greater than or equal to the saturated permeability, or if the duration is long enough to fully saturate the slope (Fredlund (2012)). $I_z \approx 0.14 \cdot k_{sat}$, so steady state ($i = I_z/k = 1$) infiltration happens at the pressure level corresponding to $k_{rel} = 0.14$ in Figure 2.7 (a). In the steady state infiltration zone, the pore pressure $-u_w$ remains unchanged with time. The slope of the pressure profile is directly related to the slope of the hydraulic gradient

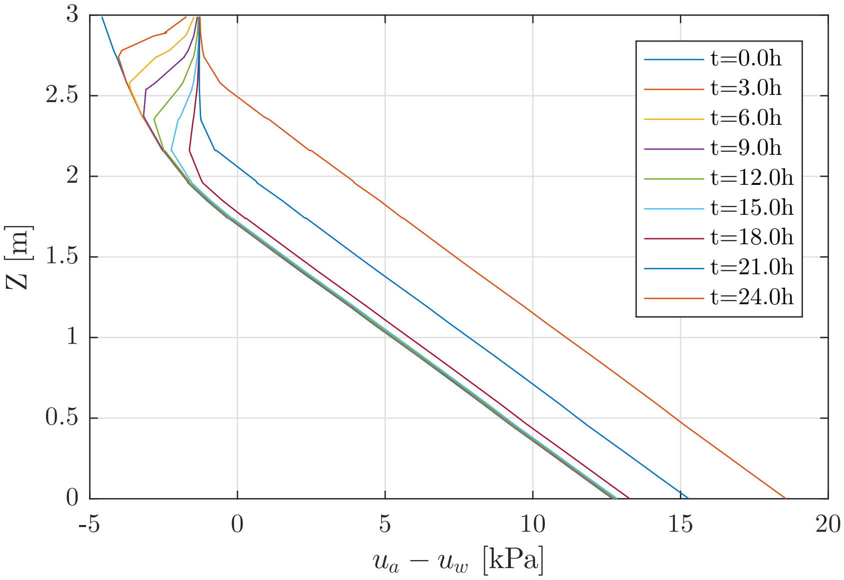

Figure 2.8: *Pore pressure profiles under rainfall infiltration calculated with the numerical model, at time intervals of 3 hours.*

at that point (Fredlund (2012)). The gradients near surface are the greatest in the beginning of infiltration, when k_{rel} is lowest. The GW-table starts to rise around $t = 18$ h when enough infiltrating rainwater reaches the capillary zone. At $t = 24$ h, the pore pressure increase relative $t = 0$ is 5.87 kPa beneath the raised GW-level.

Figure 2.9 shows the degree of saturation, from left: after the steady state (t =0 h), mid transient groundwater analysis (t =12 h) and after the transient groundwater analysis (t =24 h).

The profile in focus is the middle section of the slope (Ref. Figure 2.6), and the blue line defines the GW-table. Here, it can be observed that at $t = 0$ h, the degree of saturation in the unsaturated zone interpreted from the SWCC function ranges between 60% and 100%. During infiltration, the upper part of the zone saturates during steady state infiltration, as shown in the middle figure. The last profile to the right shows that, with an initial H_w of 1.5 m, the 24 hour long 60 mm/day rainfall nearly saturates the profile. 100% saturation situation and ponding on the surface is not reached during this simulation.

In Figure 2.10 three profiles of relative permeability are shown, calculated at t =0 h, t =12 h and t =24 h. The profiles illustrate that initial permeability of the soil is significantly reduced in the unsaturated zone, as determined by the Van Genuchten permeability function in Figure

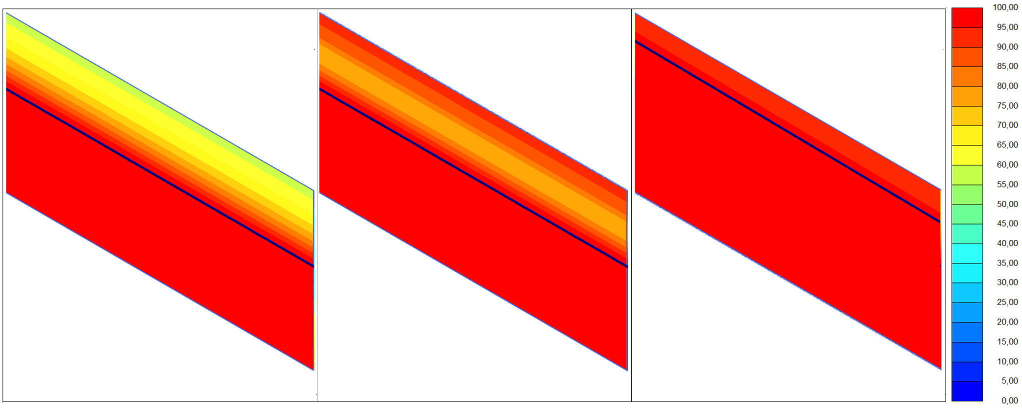

Figure 2.9: *Degree of saturation, from left: after the steady state (t=0 h), mid transient groundwater analysis (t=12 h) and after the transient groundwater analysis (t=24 h).*

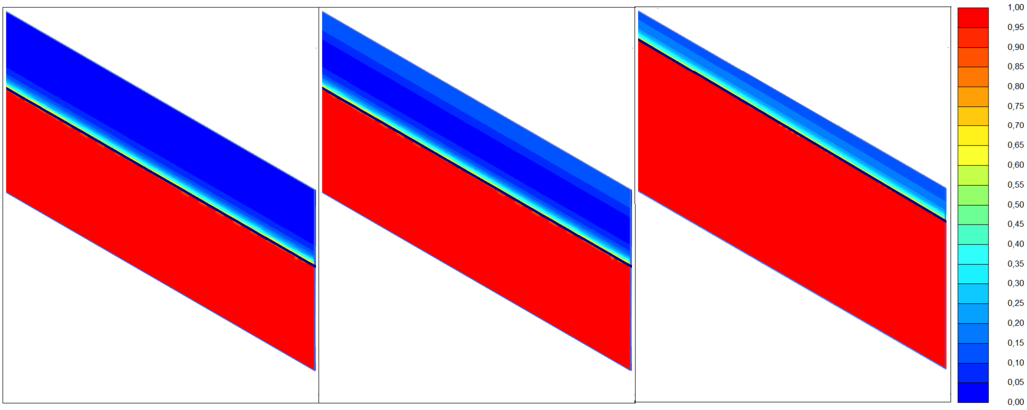

Figure 2.10: *Relative permeability,from left: after the steady state (t=0h), mid transient groundwater analysis (t=12h) and after the transient groundwater analysis (t=24h).*

2.7 (a). As discussed previously, during steady state infiltration, the relative permeability will be $k_{rel} = I_z/k_{sat} = 0.14$. This is illustrated in the upper parts of the middle (t =12 h) and right (t =24h) profiles in Figure 2.10. On the scale to the right, middle light blue colours correspond to k_{rel} values around 0.1 to 0.2.

Lastly, Figure 2.11 on the next page shows the directions of calculated groundwater seepage pattern in the unsaturated part of the soil at $t = 12$ h. In the bottom left corner, the GW-table with slope parallel flow in the saturated zone below is apparent. Some slope parallel flow is also observed above the GW-table in the capillary zone, consistent with field observations described in

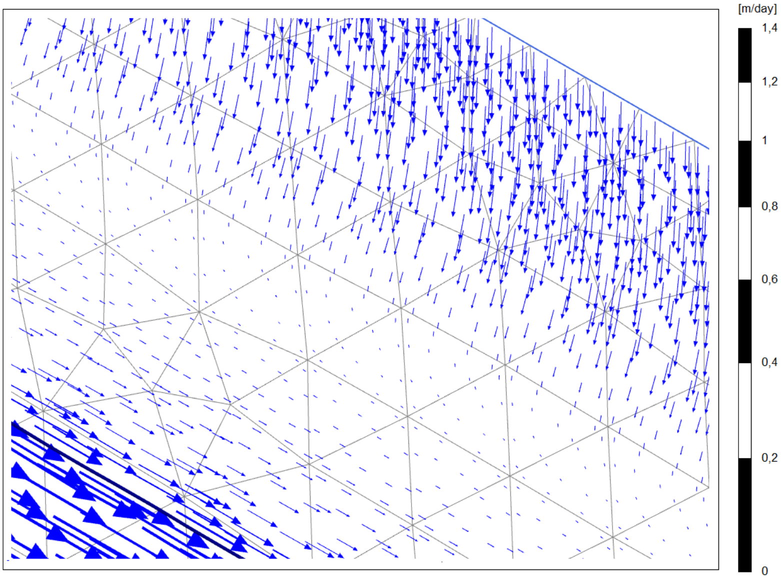

Figure 2.11: *Directions of infiltrating rainwater and GW flow at* $t = 12\ h$ *in the transient groundwater analysis*

literature (Lars Lundin (1990a)). The top right part of the figure shows infiltration of rainwater in the unsaturated zone. Equations 2.1 and 2.2 can be used to explain the directions of the flow: water flows from a higher to lower potential. Near the surface, steady state infiltration has developed, as discussed above. In the steady state infiltration zone the pressure does not change with soil depth Z, so the direction of the flow in straight downward towards lower depths. The flow is elevation driven. Ahead of the infiltration front in the unsaturated zone, the pressure is lower (Ref. Figure 2.8). Here, the hydraulic gradient, $i = I_z/k$, increases as the water infiltrates down in parts of the soil with lower permeability (Ref. Figure 2.10), and the direction of flow changes.

The results discussed above show that the numerical model is able to model many important and complex features of unsaturated groundwater flow theory. It is thus well suited for detailed studies of rainfall-induced landslides, for instance when the time to failure during a rainfall event is of interest. In the probabilistic study of rainfall induced landslides in this thesis, the implementation of this numerical model is included in order to examine how the results obtained potentially differ from results obtained with a simpler analytical model.

2.3 Slope stability models

In the slope stability evaluation part of the rainfall-induced landslide analysis, two different methods for calculating factors of safety are implemented. In the analytical analysis, a limit equilibrium equation is used, and in the numerical analysis, a finite element model and numerical stability analysis is implemented in Plaxis 2D. Both methods are based on the Mohr-Coulomb failure criterion. The following section briefly presents the Mohr-Coulomb failure criterion for saturated and unsaturated soil. Subsequent, the analytical and numerical stability models are explained.

2.3.1 The Mohr-Coulomb model

The Mohr-Coulomb model is a well known linear-elastic perfectly plastic approximation of soil behaviour (e.g. Plaxis (2016c)). The Mohr-Coulomb failure criterion can describe the shear strength of a saturated soil:

$$\tau_{ff} = c' + (\sigma_f - u_w)_f \tan\phi' \tag{2.12}$$

where τ is shear stress on the failure plan at failure. c' is effective cohesion, which is the shear strength intercept when the effective normal stress, $(\sigma_f - u_w)$, on the failure plane is equal to zero. u_w is pore-water pressure at failure and lastly, ϕ' is effective internal friction angle, characterizing the increase in shear strenght due to an increase in net normal stress. The subscript f indicates the failure stress condition at the failure plane.

The Mohr-Coloumb criterion was extended to embrace unsaturated soils by Fredlund et al. (1978). The shear strength equation for unsaturated soils can be written as follows:

$$\tau_{ff} = c' + (\sigma_f - u_a)_f \tan\phi' + (u_a - u_w)_f \tan\phi^b \tag{2.13}$$

where c' is effective cohesion, intercept of the extended failure envelope on the shear stress axis, where net normal stress and suction at failure are equal to zero. u_a is pore-air pressure, $(u_a - u_w)_f$ is matric suction on the failure plane at failure. ϕ^b is an angle characterizing the increase in shear strength due to an increase in matric suction. It can be expressed in terms of Bishops matric

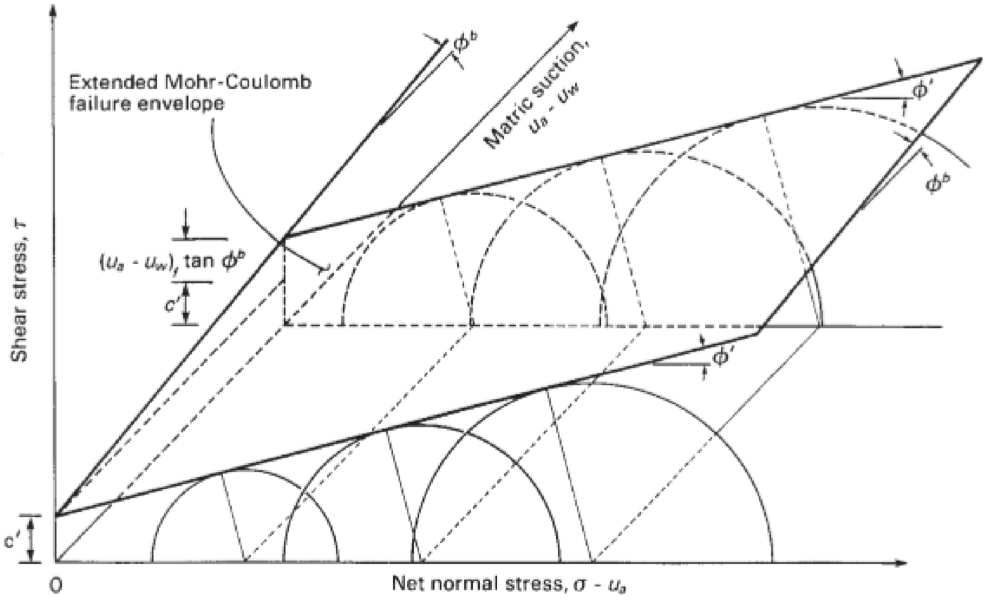

Figure 2.12: *Illustration of the extended Mohr Coulomb failure criterion from Fredlund (2012)*

suction coefficient χ: $\tan\phi^b = \chi\tan\phi'$(Fredlund (2012)). χ is a soil parameter related to the degree of saturation, part of the oldest and most-often-referred to effective stress relationship for unsaturated soils proposed by Bishop et al. (1960)):

$$\sigma' = \sigma - u_a + \chi(u_a - u_w) \tag{2.14}$$

and it is often given by: $\chi = S_{\text{eff}} = (\frac{S-S_{res}}{1-S_{res}})(u_a - u_w)$ (Plaxis (2016b)).

The transition between (2.13) and (2.12) goes smoothly as u_w approaches u_a as the soil approaches saturation and $u_a - u_w$ becomes zero. Figure 2.12 illustrates the extended failure envelope and how it increases with increasing matric suction in unsaturated soil.

2.3.2 Analytical stability model

Stability of rainfall-induced landslides slopes can be evaluated with an one dimensional limit equilibrium infinite slope model. Recall Figure 2.3 (b) illustrating the defined slope geometry in Iversons model. In the infinite slope model, all forces not resolvable on planes parallel to the slope surface are neglected. The shallow failure surface is assumed slope parallel, and the sliding soil block infinitely long and wide, so that stresses on two planes perpendicular to the slope are collinear, equal in magnitude, opposite in direction and can therefore be ignored. Milledge et al. (2012) argues that these assumptions are reasonable for landslides with L/H ratios of 25, but too conservative for smaller L/H ratios. This corresponds well to reported ratios in rainfall-induced slope failures observed in Norway (NVE (2013)). Thus, use of the infinite slope models in analysis of rainfall induced slope stability can be justified, and is often preferred for simplicity (Zhang et al. (2011)).

Failure in the infinite slope model is described by an equation that balances the slope parallel component of gravity driven stress against the resisting Mohr-Coulomb friction stress. Based on the extented Mohr-Coulomb failure criterion (Fredlund et al. (1978)), the factor of safety for the slip surface at depth Z in a unsaturated uniform soil slope, can be calculated by Cho and Lee (2002):

$$F_s = \frac{c' + (u_a - u_w)\tan\phi_b + (\sigma - u_a)\tan\phi'}{\gamma_s Z \sin\theta\cos\theta} \tag{2.15}$$

Here, the numerator is equal to 2.13, the unsaturated strength of the soil. $\sigma - u_a$ is the net normal stress on the slip surface, and $\gamma_s = \frac{\gamma_w}{1+e}(G_s + eS)$ is the total unit weight of the soil at the given depth, were S, e and G_s is the saturation, the void ratio and the specific gravity, respectively.

By simplifying; $\sigma - u_a = \gamma_s Z \cos^2\theta$, $u_a - u_w = -h_p\gamma_w$ and $\phi^b = \phi'$, Iverson (2000) and Cho and Lee (2002) presented a safety factor equation for different pore water pressure profiles, here in the time dependent formulation implemented in this thesis:

$$F_s(Z,t) = \frac{c'}{\gamma_s Z \sin\theta\cos\theta} + \frac{\tan\phi'}{\tan\theta} - \frac{h_p(t)\gamma_w\tan\phi'}{\gamma_s Z\tan\theta} \tag{2.16}$$

With this equation, factors of saftey at all dephts Z and times t during rainfall infiltration can be found, using the pressure head conditions predicted with Equations (2.9a) to (2.11c). The depth Z that first yields $F_s = 1$ determines the landsliding depht. This equation avoids specification of a GW-table depht, the position of which is irrelevant mechanically if the pressure head distribution is known. This is, of course, with the exemption of the subtle influence on $\gamma_s = \frac{\gamma_w}{1+e}(G_s + eS)$. A conservative solution is to specify $S = 1$ for all (Z,t).

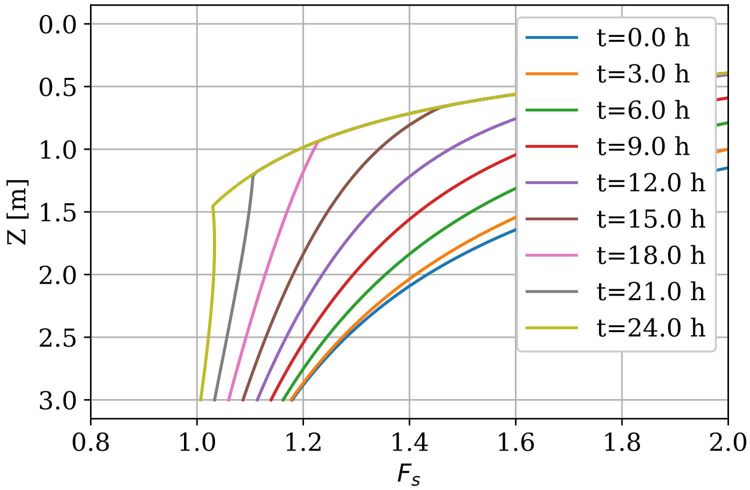

Figure 2.13: *Performance of the implemented analytical stability model*

Figure 2.13 shows values of $F_s(Z, t)$ calculated for the pore pressure development in Figure 2.8. Recall that calculation is done for a 3m high slope with $\theta = 25$ degrees and GW-table depth $H_w = 1.5$ m. The soil properties are defined as the mean values presented later in Table 4.1 (Section 4.3).

2.3.3 Numerical stability model

A numerical slope stability model is implemented in Plaxis 2D, using a Mohr-Coulomb drained material model for the soil. The linear elastic perfectly plastic model uses a simple constant description of stiffness, with no consideration of stress-dependency of the stiffness modules. Due to this, computations tend to be relatively fast, making the Mohr-Coulomb model an efficient choice (Plaxis (2016a)). The disadvantage is that the model can underestimate soil strength, but for the purposes of the probabilistic study of this thesis, this limitation is acceptable. Unsaturated behaviour and suction is taken into account using Bishops stress (1960) in the extended Mohr-Coulomb failure criterion (Fredlund et al. (1978)).

The stability model shares geometry and mesh democratization with the Plaxis 2D rainfall infiltration model, as presented in Figure 2.6. The maximum slope thicknesses used in the study are around H =2 m, so the slope length is chosen as $L/\cos\theta = 50\cos\theta$ m, giving a minimum value $\approx$ 47 m for $\theta = 20°$. This assures that the ratios of slope thickness to slope lengths are $H/L \sim 1/20$, about the same range that was suggested by Griffiths (2010). As shown in Figure 2.6, the numerical model slope is divided into three main sections, the central section spanning a horizontal distance of $0.7L$, and outer sections spanning horizontal distances of $0.15L$. The boundary conditions are specified such that displacements on the bedrock interface boundary $\Gamma 1$ are fixed in all directions. Displacements on the slope beginning and end boundaries $\Gamma 3$ are fixed in the horizontal direction, while no restriction of movement is set on the slope surface $\Gamma 2$.

In the stability model, slightly higher strength is assigned to the outer sections soils to force slope failure to occur in the central section with the actual soil strength. This is a solution implemented to avoid numerical instabilities from occurring at the model boundaries and to minimize effects of the end fixities on estimated slope stability. Furthermore, increased mesh refinement is applied in middle section where results are studied.

Stability of the slope in the numerical analysis is expressed in terms of a global safety factor F_s. The F_s value is obtained in a Safety calculation phase specified below, with an algorithm where the shear strength parameters $\tan\phi'$ and c' are successively reduced until slope failure occurs. The factor of safety is given by:

$$F_s = \frac{\text{available strength}}{\text{strength at failure}} = \frac{\tan\phi_{input}}{\tan\phi_{reduced,f}} = \frac{c'_{input}}{c'_{reduced,f}} = \frac{\text{Tensile strength}_{input}}{\text{Tensile strength}_{reduced,f}} \tag{2.17}$$

where the strength parameters with the subscript '$input$' refer to properties entered in the material specification in Plaxis, and the subscript $reduced, f$ refer to the reduced value at time of model failure.

The following calculation phases are used to evaluate slope stability in the numerical model:

1. Initial phase: A generation of initial effective stresses, pore pressures and steady state parameters based on slope geometry, soil parameters including K_0, the coefficient of earth pressure at rest, for total stresses and hydraulic parameters. Equilibrium of soil elements is not guaranteed.
2. Equilibrium phase: Elastoplastic drained analysis to ensure equilibrium, using pore pressure distributions h_p from the numerical steady state infiltration analysis.
3. Safety calculation phase: F_s is calculated in this phase with initial stresses and effective stresses obtained in the previous phase.

Insight in the performance of the numerical stability model is provided in Figure 2.14. Results are show for a post-rainfall safety calculation, with pore pressures calculated at $t = 24$ h in the transient numerical analysis shown earlier in Figure 2.8. The slope geometry and rainfall parameters are as specified earlier in the section on the numerical infiltration model. The plastic soil strength parameters are defined as the input mean values in the probabilistic parameter model of the case study, given in 4.1. Since the failure stage is the focus of the analysis, the soil plasticity parameters c' and ϕ' are governing of the behaviour, not the elastic stiffness parameters. Figure 2.14 (a) presents total deformations of a failed soil mass. The large deformations up slope reveals the initiation location of the slide. In Figure 2.14 (b) deviatoric strains after failure are shown. This provides insight in the position of the slip surface. It can be observed that failure is limited within the centre of the model and follows the bedrock interface. This implies that the increase in pore pressures at bedrock level was more critical for stability than the dissipation of suction at slope surface in this simulation.

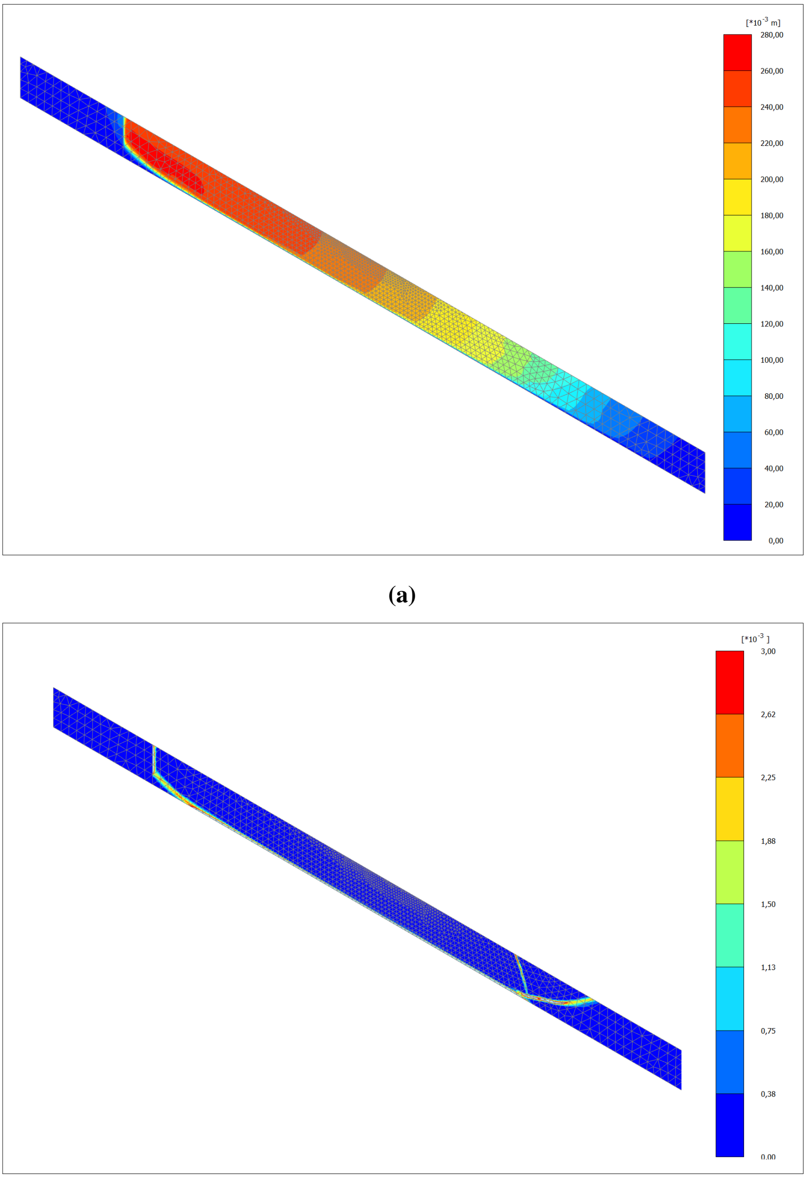

(a)

(b)

Figure 2.14: *Performance of the implemented numerical stability model: (a) Total deformations after a stability analysis in Plaxis, (b) Incremental deviatoric strain after a stability analysis in Plaxis.*

Chapter 3

Probabilistic model

3.1 Introduction

One of the main reasons for implementing probabilistic analysis for rainfall-induced landslides is the significant uncertainty associated with the problem. As in geotechnical engineering in general, most of the uncertainty reflects lack of knowledge or understanding of subsurface conditions. As a natural material formed through erosion and geological processes over millions of years, the ground is a highly variable and site specific engineering material. Its properties (e.g., strength parameters) are not uniform in space nor time. Likewise, environmental conditions (e.g., rainfall patterns) are also highly subject to spatial and temporal variability. This uncertianty is epistemic, as the subsurface conditions could, in principle, be observed. (Baecher and Christian (2003)).

The lack of information and knowledge about the geotechnical and environmental parameters driving the occurrence of rainfall-induced landslides results in uncertainties that often hinder advanced geotechnical prediction models in providing accurate predictions of landslide hazards (Zhang et al. (2011), Melchiorre and Frattini (2012)). The problem is further increased by the situation that the scope of a hazard assessment of rainfall-induced landslides often spans tens of kilometers. Additionally, systematic type of uncertainties arise with measurement and model errors. Model uncertainty reflects the inability of a model to precisely represent a system's true physical behaviour (Baecher and Christian (2003)). As discussed in Section 2.2, unsaturated flow is complex problem, and the models commonly implemented build on many assumptions, simplifications and mathematical approximations (Zhang et al. (2011), Iverson (2000)).

Currently, there is a lack of cost-efficient and reliable methods and technologies to gather information about the uncertain geotechnical and environmental parameters (Depina (2017)). For this reason there is a need to develop innovative and cost-efficient methods to reduce the uncertainties in geotechnical and environmental conditions. Development of methods that will reduce uncertainties in the geotechnical and environmental parameters has a significant potential to improve the capacity of the geotechical models to accurately predict the occurrence of rainfall-induced landslides. This will consequently help decision makers to better protect infrastructure, property and life thereatened by rainfall-induced landslides.

To contribute to this goal, this thesis aims to reduce uncertainties in geotechnical parameters controlling the occurrence of rainfall-induced landslides with the implementation of Bayesian updating. Bayesian updating is a probabilistic framework that provides a basis to integrate site specific observations with the existing (prior) knowledge on the uncertain parameters (Straub and Papaioannou (2015)). Updated uncertainties are referred as posterior knowledge. The framework addresses variability of the model soil properties and accounts rationally for various uncertainties (i.e., statistical uncertainty and measurement errors) that arise during prediction of rainfall-induced landslides.

The application of Bayesian updating for the problem of updating and reducing uncertainties in rainfall-induced landslides is advantageous because it provides a consistent and robust framework to integrate various uncertainties and observations into an updating process. The framework has been successfully applied in back-calculation of landslide controlling parameters by, among others: Ering and Babu (2016), Zhang et al. (2010) and Luo et al. (2017). Observations of slope performance represent an important source of additional information that can be used to update and reduce uncertainties. A key motivation for using observations of slope performance in Bayesian updating originates from the low cost that will be required to gather such information in comparison to more conventional methods for collecting data on uncertain geotechnical parameters.

3.2 Probability theory

3.2.1 Random variables

A few relevant concepts used in statistics are presented in the following. The theory and equations are adapted from the book *Reliability and Statistics in Geotechnical Engineering* by Baecher and Christian (2003) unless other references are given.

When soil parameters are modeled as *random variables*, this does not mean that site characteristics in reality are assumed to be caused by chance. On the contrary, as stated above, the spatial distribution of soil structure and material properties is very much fixed and could, in principle, be observed. Rather, for the sake of modelling, they are treated as random.

Statistical methods are based on probability theory. The mathematical theory of probability deals with experiments and their outcomes. The set of all possible outcomes of an experiment is called the sample space, Ω. Individual outcomes are called sample points, and possible values of a random variable can be single sample points or a set containing many points.

Random variables can have discrete or continuous sample spaces. Discrete variables typically represents counts while continuous variables represents measurements. Most random variables dealt with in geotechnical engineering, like soil parameters, will have continuous ranges since infinite values can be measured.

3.2.2 Probability density functions

Parameters that are handled as random variables can assume numerical values given by their probability distributions. For continuous variables, this function is called a Probability Density Function (PDF). In this case, probability is dealt with as a density and found by integrating the probability mass over a finite region of the sample space:

$$P(x_1 \leq X \leq x_2) = \int_{x_1}^{x_2} f_X[x]dx \tag{3.1}$$

Here, $f_X[x]dx$ is the probability that X is in an infinitesimal range around x of width dx. For continuous variables, the probability that the value of X is exactly some given value x_0, $P(X = x_0)$, is zero.

The integral of the PDF over the sample space is

$$\int_{\Omega} f_X[x]dx = \int_{-\infty}^{+\infty} f_X[x]dx = 1 \tag{3.2}$$

Distribution parameters

Different measures of central tendency and variability can be used to describe distributions. The most common ones are: mean μ, standard deviation σ[1] and coefficient of variation, CoV. The mean is a measure of the central tendency of a distribution. For a set of n data $x = [x_1...x_n]$, the estimate of the mean is:

$$\bar{\mu} = \frac{1}{n}\sum_{i=1}^{n} x_i \tag{3.3}$$

Standard deviation is a measure of dispersion, with the following estimate:

$$\bar{\sigma} = \sqrt{\frac{\sum_i^n (x_i - \bar{x})^2}{n}}, \tag{3.4}$$

and CoV expresses relative dispersion, with the estimate defined as

$$CoV = \frac{\bar{\sigma}}{|\bar{\mu}|}. \tag{3.5}$$

where $\bar{\mu} \neq 0$.

Probability distributions

The five distributions used in this analysis are as follows:

1. Normal distribution

The Normal distribution is a good approximation for how many geotechnical variables are distributed. It describes variables with symmetrically and exponentially distributed outcomes around some mean value, μ. For a variable X, the PDF is defined as

$$f_x(x \mid \mu, \sigma) = \frac{1}{\sigma\sqrt{2\pi}} e^{-\frac{1}{2}(\frac{x-\mu}{\sigma})^2}. \tag{3.6}$$

---

[1] In this chapter, σ is always the symbol for standard deviation, not normal stress.

2. Lognormal distribution

The lognormal distribution is commonly used for modeling positive variables and variables that vary over several orders of magnitude. If X is lognormally distributed, then $Y = \ln(X)$ is normally distributed. The PDF is defined as:

$$f_x(x \mid \mu_Y, \sigma_Y) = \frac{1}{X\sigma_Y\sqrt{2\pi}} e^{-\frac{1}{2}(\frac{\ln(x)-\mu_Y}{\sigma_Y})^2}, \tag{3.7}$$

where μ_Y and σ_Y are the parameters of the underlying normally distributed Y.

3. Uniform distribution

This is a continuous distribution defined between a minimum and maximum value, where all outcomes have equal probability. The PDF is simply given by:

$$f_x(x) = \frac{1}{b-a}, \quad a(\text{min}) \leq X \leq b(\text{max}). \tag{3.8}$$

where a and b are the minimum and maximum value, respectively.

4. Multivariate normal

The multivariate normal distribution is a generalization of the one-dimensional normal distribution (3.6) to higher dimensions (e.g. Baecher and Christian (2003)).

Functions of random variables

A function $\mathbf{Y} = g(\mathbf{X})$ can be formulated where $\mathbf{X} = [X_1, X_2, \ldots, X_n]^T \in \mathbb{R}^n$ is a vector of random variables (e.g., n random soil properties) associated with the joint PDF, $\mathbf{X} \sim f(\mathbf{x})$. $\mathbf{x}$ is a realization of $\mathbf{X}$ in the corresponding outcome space Ω_X. $\mathbf{Y} = [Y_1, Y_2, \ldots, Y_m]^T \in \mathbb{R}^m$ is then the vector of random response (e.g., displacements at m locations in the model).

Uncertainty quantification in cases where $\mathbf{Y}$ is a non-linear combination of multiple variables is often difficult to perform. Problems of this kind is therefore commonly solved with approximate methods or sampling methods.

3.3 Bayesian updating framework

3.3.1 Basic principles

The Bayesian framework provides methods for revising uncertainties in engineering systems based on information of the system performance.

The Bayesian updating method starts with a prior probability or probability distribution of one or multiple random variables. This is the *a priori* hypothesis. Updated *a posteriori* probabilities or distributions of probability accounting for new information can then be calculated with Bayes's rule (e.g. (Straub and Papaioannou (2015)):

$$P(\text{hypothesis}|\text{observation}) = \frac{P(\text{observation}|\text{hypothesis})P(\text{hypothesis})}{P(\text{observation})} \tag{3.9a}$$

$$\text{Posterior} \propto \text{likelihood} \times \text{prior} \tag{3.9b}$$

$P(\text{observation}|\text{hypothesis})$ is the *likelihood function*. This is the basis for revising the probability of the hypothesis. The denominator in (3.9a) serves to normalize the total posterior probability to 1, so Bayes's rule is often expressed like (3.9b) in the context of Bayesian updating, as a statement of the proportionality of the two distributions of the hypothesis.

In reliability engineering, Bayesian analysis can be used to update an estimate of failure given new information (Straub and Papaioannou (2015)). In the following, a simple method for this is presented, based on the approach in Straub and Papaioannou (2015).

Consider a slope stability model where some parameters of the model are uncertain. These parameters are modeled as m random variables $\mathbf{X} = [X_1, ..., X_m]^{\mathrm{T}}$, characterized by their joint continuous PDF $f(\mathbf{x})$. A failure event, F, can be defined by a domain $\Omega_F = \{g(\mathbf{x}) < 0\}$ in the outcome space of $\mathbf{X}$. $g(\mathbf{x})$ is the performance function, typically defined in terms of the factor of safety $g = F_s - 1$. The probability of failure is evaluated by $P(F) = P(g(\mathbf{X}) < 0)$. This can be illustrated in Figure 3.1. Here, a failure event $\Omega_F = \{g(\mathbf{x}) < 0\}$ in the outcome space of the joint continuous PDF $f_X(\mathbf{x})$ of two random variables x_1 and x_2 is shown. Probability of failure is equal to the probability of all outcomes in the failure domain.

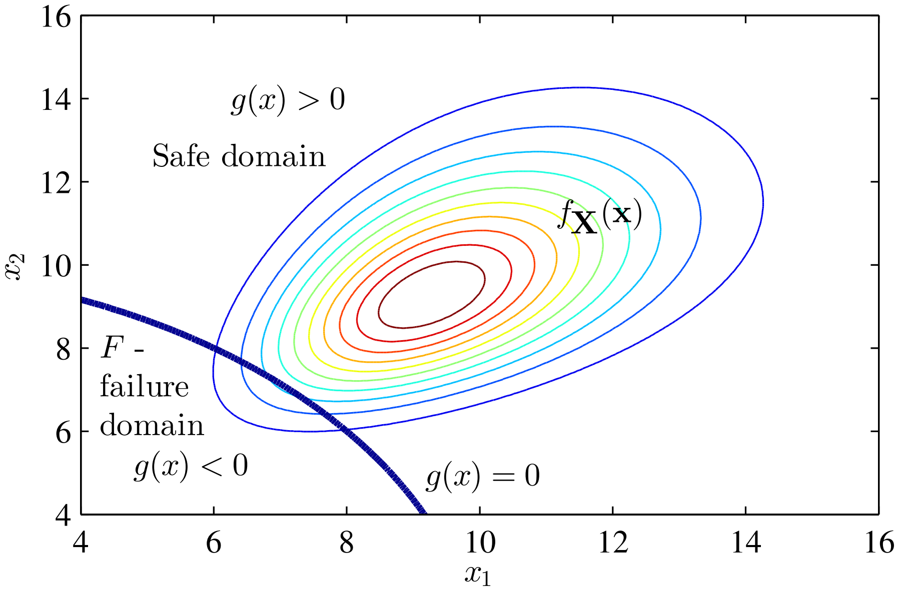

Figure 3.1: Illustration of the performance function (Credit: Ivan Depina)

Also, assume that an observation of slope stability is available, considered event ϵ with Ω_ϵ. Updated failure probability given ϵ can be calculated with the following equation, an alternative way to formulate Bayes's rule (Straub and Papaioannou (2015)):

$$P(F|\epsilon) = \frac{P(F \cap \epsilon)}{P(\epsilon)} \tag{3.10}$$

where $(F \cap \epsilon)$ is the intersection of sets F and ϵ, meaning a set that contains all F that also contains ϵ.

Bayes's rule can also be applied to update probability densities. Still considering a slope stability model with m random variables $\mathbf{X}$, the updated *a posteriori* probability distribution of the parameters can be found by reformulating (3.9a) (Straub and Papaioannou (2015)):

$$f(\mathbf{x}|\epsilon) = \frac{P(\epsilon|\mathbf{x})f(\mathbf{x})}{\int\limits_{-\infty}^{+\infty} P(\epsilon|\mathbf{x})f(\mathbf{x})d\mathbf{x}} = c \cdot L(\mathbf{x}) \cdot f(\mathbf{x}) \tag{3.11}$$

Here, $P(\text{hypothesis}|\text{observation}) = P(\mathbf{x}|\epsilon) = f(\mathbf{x}|\epsilon)d\mathbf{x}$, $P(\text{hypothesis}) = f(\mathbf{x})d\mathbf{x}$ and $L(\mathbf{x}) \propto P(\epsilon|\mathbf{X} = \mathbf{x})$ is the likelihood function, proportional to the probability of observing a given value of model parameters. $P(\text{observation}) = P(\epsilon)$ is computed by the integral in the denominator, and ensures that the posterior distribution is proper, that is, integrates to one.

One of the central elements in the Bayesian Framework is formulation of the likelihood function. In the context of engineering reliability updating, observations of new information typically corresponds to outcomes of the models. The observation domain Ω_ϵ can be defined trough a limit state function $h(\mathbf{X})$, representing the observation in terms of the stability model F_s. (Straub and Papaioannou (2015)).

The new information can be of either the inequality type, if written as $h(\mathbf{x}) \leq 0$, or the equality type, if written as $h(\mathbf{x}) = 0$. If all new observations are of the first type, computation of (3.11) and (3.10) is straightforward using sampling methods (ref. Section 3.3.2). However, if the new information is of the second type, it cannot be implemented as easily. When dealing with continuous distributions, the probability of something taking on a specific value will be zero. This problem can be solved by transforming the equality information into the inequality type (Straub and Papaioannou (2015)).

3.3.2 Bayesian updating using Monte Carlo sampling methods

Generally, derivation of exact solutions of (3.10) and (3.11) is not possible because this often involves solving high dimensional integrals (Baecher and Christian (2003)). Various sampling methods are often implemented when the models used are nonlinear, complex, or involves several uncertain parameters. Implementation of sampling methods allows for estimation of the probability distributions of the output variables given the probability distributions of the input random variables and updating information.

Updating probabilities and distributions with sampling methods

A simple approach for updating probabilities and distributions using a direct Monte Carlo simulation (MCS) method is explained in the following. MCS are numerical processes of repeatedly calculating a mathematical/empirical operator, where the variables within the operator are random or contain uncertainties with prescribed probability distributions (Baecher and Christian (2003)).

Considering again a slope stability model where some parameters of the model are uncertain. These parameters are modeled as m random variables $\mathbf{X} = [X_1, ..., X_m]^{\mathrm{T}}$, characterized by their joint continuous PDF $f(\mathbf{x})$. A failure event, F, defined by a domain $\Omega_F = \{g(\mathbf{x}) < 0\}$ in the outcome space of $\mathbf{X}$. $g(\mathbf{x})$ is the performance function, defined in terms of the factor of safety $g = F_s - 1$. The process starts with evaluation of $g(\mathbf{x})$ for n_{MC} random realizations of $\mathbf{X}$ sample sets. Probability of failure will simply be the ratio of failed samples over the total number of samples.

New information ϵ, defined $h(\mathbf{x}_{obs} < 0])$, is to be introduced in the Bayesian updating process. When re-evaluating the prior input failure probability and parameter distributions, all simulations disagreeing with the observation are erased. Equation (3.10) for calculating the updated failure probability reduces to:

$$P(F|\epsilon) = \frac{\sum_j I[g(\mathbf{x}) < 0] \cdot I[h(\mathbf{x}_{obs}) < 0]}{\sum_j I[h(\mathbf{x}_{obs}) < 0]} \tag{3.12}$$

where I is the indicator function, simply taking the value 1 if the statement within the brackets is true, and 0 otherwise.

After non-observed simulations are removed, the simplest way of estimating the updated distributions is to form histograms of the remaining parameter realizations. However, when $P(F|\epsilon)$ is low, resampling techniques must be applied in order to get representable results.

Subset simulation

In this thesis, a sampling technique proposed by Au and Beck (2001) called Subset simulation is used. A well written explanation of the approach in a geotechnical engineering context is given in Cao (2017). The motivation for applying this sampling technique, and the basic elements of it is explained in the following.

Subset simulation is proposed as an effective alternative to the simple direct MCS. Although direct MCS has advantages such as easy implementation, a major disadvantage of the technique is slow convergence rates. This is a typical issue when dealing with relatively small probabilities, because the number of simulations necessary to ensure desired calculation resolution can be very high. Again referring to Figure 3.1; if the failure probability is small, the ratio of samples generated in the failure domain over total number of samples will be very low. Thus, the calculated posterior probabilities based on these samples can be misleading. Furthermore, when sampling parameters for advanced numerical models, such as the models presented in Sections 2.2.4 and 2.3.3, each model evaluation is computationally costly and the number of simulations should thus be minimal.

The basic idea of subset simulation is to express a small probability as a product of larger conditional probabilities by introducing intermediate failure events (Au and Beck (2001)). The rare event simulation problem is converted into a sequence of reliability problems corresponding to more frequent conditional probabilities. Consider a slope stability problem where F_s is the critical response and the probability of F_s smaller than a given value ”fs” is of interest. let $fs = fs_m < fs_{m-1} < ...fs_2 < fs_1$ be an increasing sequence of m intermediate threshold values. The probability of $P_f = P(F_{s,i} < fs)$ can be written (Au and Beck (2001)):

$$P_f = P(F_1) \prod_{i=2}^{m} P(F_i|F_{i-1}) \tag{3.13}$$

where $F_{s,i}$ is the ith intermediate event. In implementation, the fs_i values are determined adaptively, corresponding to the specified value of a conditional probability p_0. The value of p_0 is limiting state chosen to assure desired accuracy in the results. $p_0 = 0.1$ is found to be a good choice (Au and Beck (2001)). For instance, if one is interested in finding a small failure probability, the limit state of the iterative subset simulation sampling process is reached when 10% of the samples are failures.

Subset simulation makes use of a specially designed Markov Chain MCS (MCMCS) technique for simulating samples according to an arbitrary probability distribution in each iteration. MCMCS is a numerical process that provides a feasible way to conditionally generate samples from an arbitrary PDF. A well written explanation of the of the MCMCS algorithm and Subset Simulation process in a geotechinal context is provided in Cao (2017).

Subset simulation updating process

In the following, a brief explanation of the Bayesian Updating process of this thesis, using direct MSC and Subset Simulation techniques, is presented. Figure 3.2 on the following page is provided as an illustration of the iterative process of subset simulation in a slope stability prediction.

First, n_{MC} sets of randomly generated values for some given uncertain parameters are created

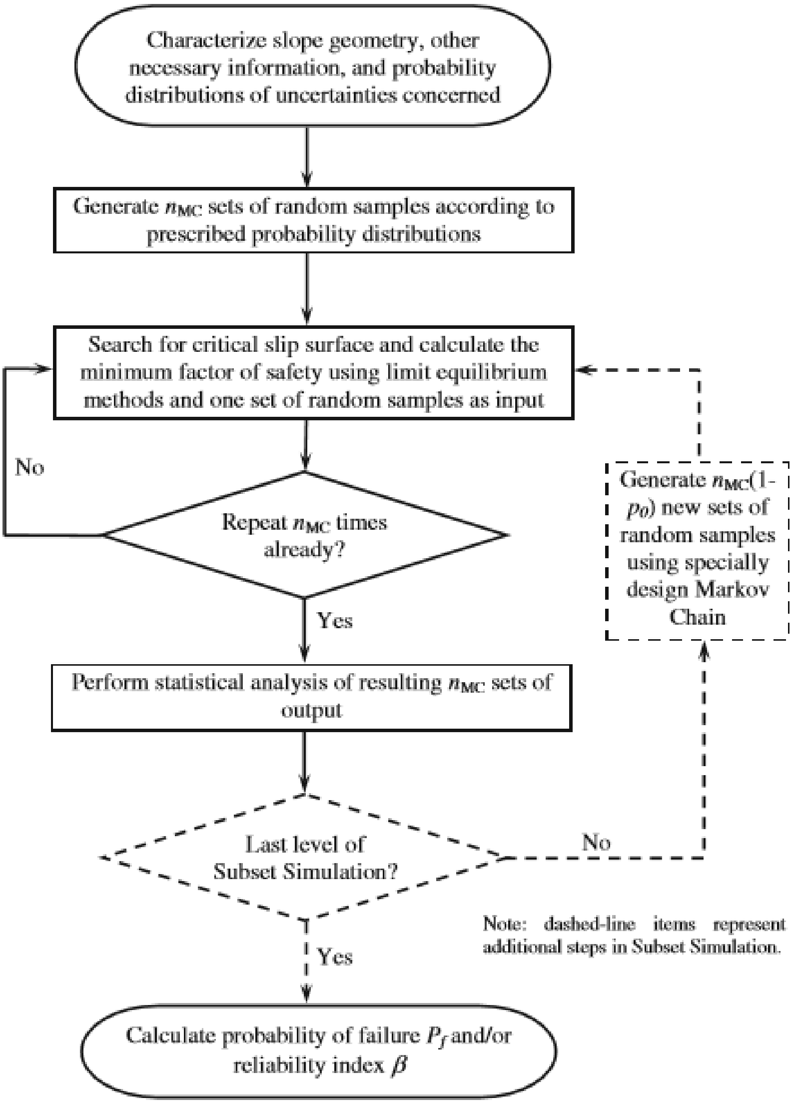

Figure 3.2: *Flowchart for Subset simulation of slope stability analysis (Credit: Wang et al. (2011)).*

using direct MCS (Baecher and Christian (2003)). The values are generated from the parameters' given prior probability distributions. The considered model or performance function is computed for each set. If, for instance, a limit state function is defined: $g(\mathbf{X}) = F_{s,\text{initial}}(\mathbf{X}) - 1$, probability of failure is simply $P(F) = P(g(\mathbf{x}) < 0) = \frac{I}{n}\sum_j I[g(\mathbf{X}_j) < 0]$, where I is the indicator function that takes the value 1 if $g(\mathbf{x}) < 0$ and zero otherwise. Referring to Figure 3.1, this means the ratio of samples generated from within the failure domain, over the total number of samples generated in the outcome space. This limit state function then corresponds to an observation of slope failure, that is used to update the prior distributions of the model input parameters **X**.

The procedure of Subset Simulation starts with ranking the outcomes, F_s values, of the n_{MC} samples. If $p_0 n_{MC}$ values are in the desired failure domain $(g(\mathbf{x}) < 0)$, the limit state is reached. If not, the $(1 - p_0)n_{MC}$th value in the ascending list of F_s values is chosen as fs_i, and hence, the sample estimate for $P(F_1) = P(F_s > fs_1)$ is always p_0. In other words, there are $p_0 n_{MC}$ samples with $F_1 = F_s > fs_1)$ among the samples generated by direct MCS. Then, starting from the $p_0 n_{MC}$ samples with $F_1 = F_s > fs_1)$, MCMCS is used to simulate $(1 - p_0)n_{MC}$ additional conditional samples given $F_1 = F_s > fs_1)$, so that there are a total of n_{MC} samples with $F_1 = F_s > fs_1)$. Now, a ranking of values and check if limit state is reached is done again. The iterations continue until the limit state, or a limiting number Subset Simulation iterations m, is reached (Ref. figure 3.1). In total, the subset simulation procedures contains $m + 1$ steps, including one direct MCS to generate unconditional samples and m steps of MCMCS to simulate conditional samples. This generates a total of $n_{MC} + m(1 - p_0)n_{MC}$ samples (Au and Beck (2001)).

By the completion of the process explained in these two previous sections, a description of the prior-to-updating situation is generated, in terms of model parameter distributions and factors of safety. If desirable, the prior probability of failure can now be calculated (Ref. figure 3.1).

The next step in the Bayesian updating procedure is sampling from the posterior parameter distributions. In other words, generating samples corresponding to the observation information of slope failure. The simple way of doing this is directly selecting all realized samples in the failure domain and form the updated distributions or histograms solely based on these. However, if the failure probability is small, the number samples may not be sufficient to give representative distributions. For comparison of prior and posterior factors of safety and model parameter values it is typically desirable that the prior and posterior amount of samples are the same. MCMCS and Subset Simulation can then be applied again to simulate conditional samples of parameters based on the realized failure samples (Au and Beck (2001)). Lastly, posterior probabilities of failure can be calulated.

Chapter 4

Kvam Case Study

4.1 Introduction

A case study is implemented to evaluate the performance of the studied prediction models, and the effect of the Bayesian updating framework on rainfall-induced landslide safety assessment. The case study is based on landslide events that occurred in 2011 and 2013 in the Kvam area, Gudbrandsdalen, Norway. Information on the geotechnical, hydrological and climate conditions that lead to the occurrence of the landslide events in 2011 is gathered as background for the input parameters in the probabilistic study. The lack of field measurements of geotechnical and hydraulic parameters is an important motivation for investigating if something can be learned about the cite conditions from doing a probabilistic Bayesian analysis. The aim of the site specific case study is to gain additional insights in the different factors controlling the occurrence of rainfall-induced landslides in the Kvam area, Gudbrandsdalen.

In the first following sections, descriptions of the Kvam site and 2011 landslide event are given. Selected probabilistic models and input parameters are presented and, lastly, the case study approach is explained.

4.2 Description of study area

Gudbrandsdalen is an area prone to landsliding and debris flows over the course of history (Walberg and Devoli (2014)). Following spring snow melting and heavy rainfall on the 9.-10.06.2011, flooding, accompanied by many large slope failures and debris flows were observed in Gudbrandsdalen (Schiliro and Cepeda (2016)). Consequences of the flooding and landslides were multiple road and railroad closures, and up to 200 persons had to be evacuated from their homes. Two years later, following rainfall on the 22.-23.05.2013, landsliding activity was again observed in the area. As in 2011, road closures and evacuation followed (Walberg and Devoli (2014)). Fig-

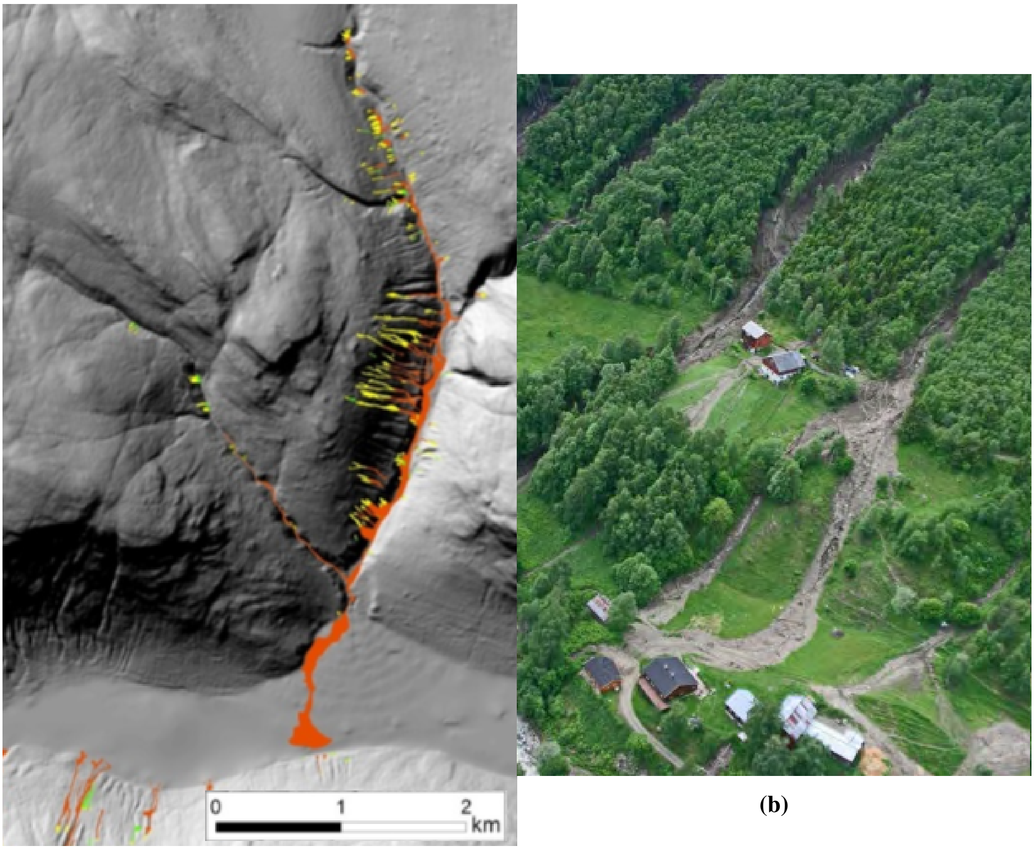

(a)

(b)

Figure 4.1: *Picture (a): Identified landslide paths and debris flows (red) and source areas (yellow)(Schiliro and Cepeda (2016)). (b): Debris flow runnout around buildings in Veikledalen (Foto: A.T. Hamarsland, NVE (2011), in Walberg and Devoli (2014)).*

ure 4.1 (a), created by NGI in 2016 based on detailed analysis of high-resolution digital elevation models (DEM's) made from aerial orthophotos, shows the active landslide paths and source areas in Veikledalen, Kvam (Schiliro and Cepeda (2016)). Picture 4.1 (b) shows debris flow run out and destruction around buildings in Veikledalen.

Geography and geology

The small town of Kvam sits surrounded by steep hillsides in Gudbrandsdalen. Figure 4.2 on the next page shows the slope angles in the area, calculated from Kartverkets 10 m terrain model.

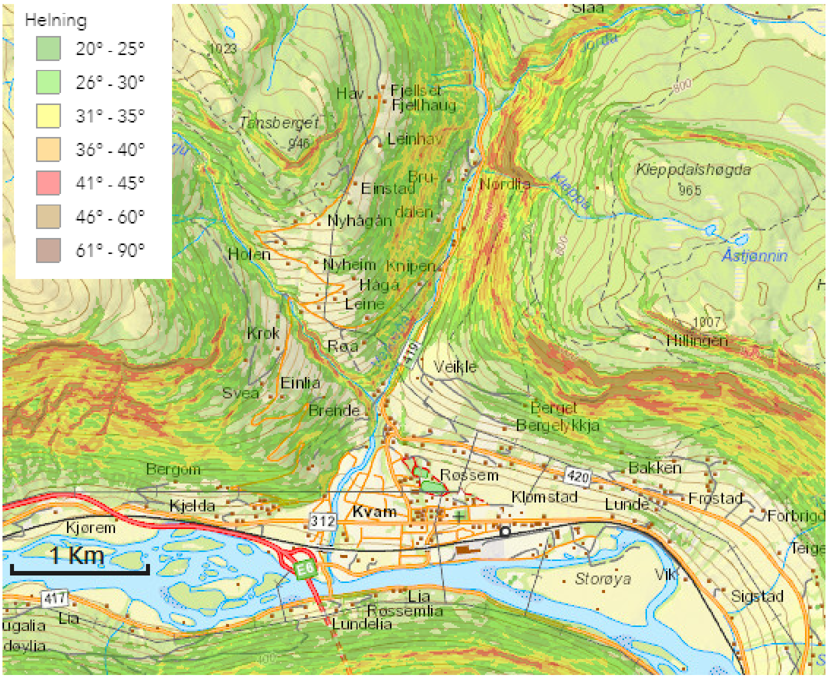

Figure 4.2: *Slope angles of the hillsides in the Kvam area (Credit: NGI.no)*

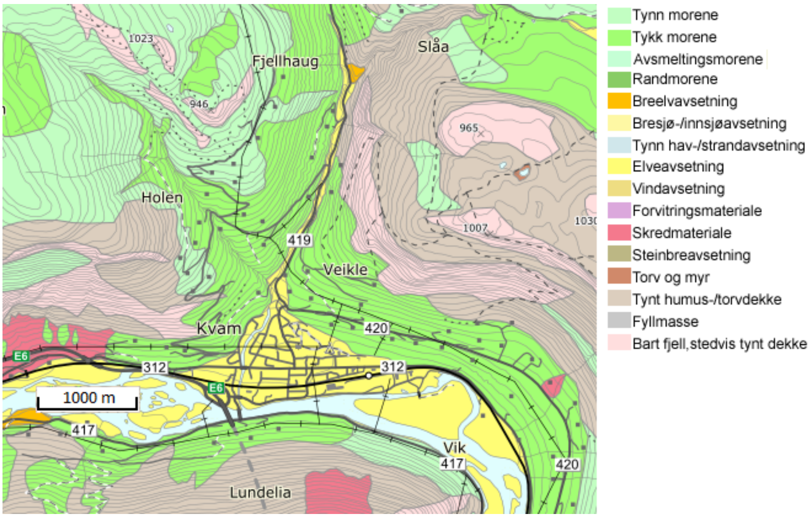

Figure 4.3: *Soil and deposits of the area. The landslides in Veikledalen were triggered west of the 419 road. Here, shades of green indicate glacial till materials. Legend from top: Thin moraine, thick moraine, melt-out moraine, end moraine. (Credit: NGU.no)*

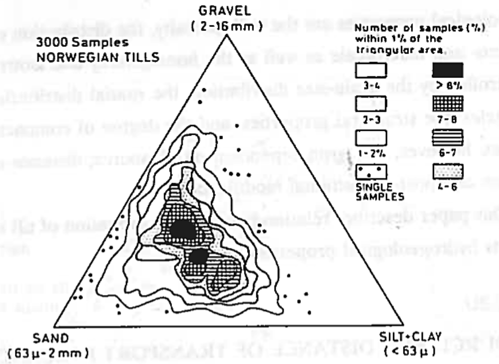

Figure 4.4: *Grain size distribution of 3000 Norwegian till samples (Credit: Jørgensen (1977))*

Large areas of the surrounding mountain plateaus and hillsides are covered by till materials deposited during the last ice age melt (Haldorsen and Krüger (1990)), as shown in Figure 4.3. Historical landslide records from Gudbrandsdalen also show that over 70% of the sliding activity in the region (i.e. all types of shallow slides, debris slides, debris flows) occurs in till deposits (Walberg and Devoli (2014)). The composition of glacial till materials can also vary significantly, but is generally unsorted and made up of all grain sizes from small clay particles to large blocks (NGU (2015)). Figure 4.4 displays the range of grain sizes found in Norwegian till samples. Although coarse-grained content may be substantial, the behaviour is generally governed by the finer fractions (Heyerdahl (2016)). Haldorsen and Krüger (1990) provides a comprehensive description of formation of Nordic till and the factors which control its hydrological properties.

4.2.1 Geotechnical properties

Strength properties of Nordic till

In general, friction of the soil increases with increasing density and roughness of the grain surface (division NTNU (2015)). In ordinary Nordic forested till, loose layers typically develop in the upper one meter of the soil, because of freezing/thawing or root and fauna activities, among other things (Lars Lundin (1990a)) In theses looser upper layers, the soil shear strength could thus be lower (Haldorsen and Krüger (1990)).

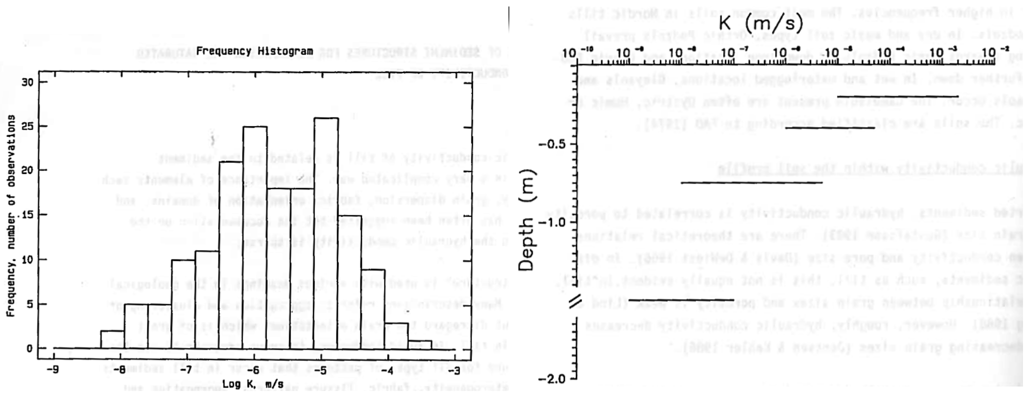

(a)

(b)

Figure 4.5: *Variations of permeability in Nordic till: (a) 190 measurements of permeability at depths of more than 40 cm in Swedish and Norwegian till with different methods (field and laboratory) (b) General variation in permeability with soil depth in till. (Credit: Lars Lundin (1990b))*

Although the strength is mainly governed by the dominating finer materials, local variations in the slopes can be considerable. The presence of big blocks and roots can have significant influence on the soil strength (Haldorsen and Krüger (1990)). Loss of shear strength due to deterioration of tree roots after felling of hill sides is a commonly reported contributing factor to rainfall-induced landslides (Edvardsen (2013), Heyerdahl (2016)).

Reported values of of friction angle in Norwegian till averages around 30° (division NTNU (2015), Melchiorre and Frattini (2012)). Reported cohesion values are typically low, around 4 kPa (division NTNU (2015), Lacasse and Nadim (1997), Melchiorre and Frattini (2012)).

Hydraulic properties of Nordic till

A general characterization of the hydraulic properties likely to be observed in the Kvam till deposit can be made based on available literature. For further details, refer to the works of J. Fredericia, B. Lind, L. Lundin, B. Lind and A. K. Høstmark et. al. presented in the comprehensive report: *Hydrogeological properties of Nordic Tills, Report No 25* by the Nordic Hydrological Programme (1990).

Permeability of sandy-silty till types in Scandinavia varies within wide limits. The heterogeneous structure makes it difficult to obtain representative values with field and laboratory methods.

Figure 4.5 (a) summarizes 190 measurements of hydraulic conductivity at depths of more than 40 cm in Swedish and Norwegian till with different methods (field and laboratory). The distribution is essentially lognormal, with a mean value of $3{\cdot}10^{-6}$ m/s. Here the great variety of observed values is also visible, ranging from $5{\cdot}10^{-9}$ to $2{\cdot}10^{-4}$ m/s. Also of great importance is the local spatial variation of permeability that can be found in a single slope. As mentioned, the upper soil layers of slopes are typically looser than the deeper layers. For this reason, permeability usually increases with depth as shown in Figure 4.5 (a) (Lundin (1982)). Furthermore, upper soil layer permeability might be locally high because of heterogeneities like cracks and macropores, even in fine-grained till where permeability usually is low (Lars Lundin (1990b)).

4.2.2 Environmental conditions

Present climate conditions

Neither Norwegian Meteorological Institute (MET) nor NVE have measurement stations in Kvam (Walberg and Devoli (2014)). Therefore, the climate data presented in this section are either measurements from the nearest meteorological weather station (MET), located in Sjoa 330 MAMSL (meters above mean sea level), 8 km north of Kvam, or geographically interpolated data from www.xgeo.no. Generally, temperatures, precipitation and snow accumulation will vary locally because of the height differences between the valley floor and surrounding hills. Some general trend observations can be made nevertheless.

The climate in Gudbrandsdalen is a typical cool continental climate with cold winters and warm summers. Because of its inland location sheltered behind Jotunheimen and the mountainous west coast, Kvam is a relatively dry area (Walberg and Devoli (2014)). Figure 4.6 shows the monthly average rainfall measured at Sjoa together with data from other neighbouring stations in Gudbrandsdalen. Figure 4.9 on page shows simulated ground saturation and precipitation interpolated at Kvam 300 MAMSL over a six year period with observed landslide activity. Saturation is simulated as the percentage ratio of the daily simulated saturation compared to the maximum simulated saturation in the period 1981-2010, using the HBV-model (www.xgeo.no). The general trend is that the groundwater supply is highest around springtime during the snow melting period.

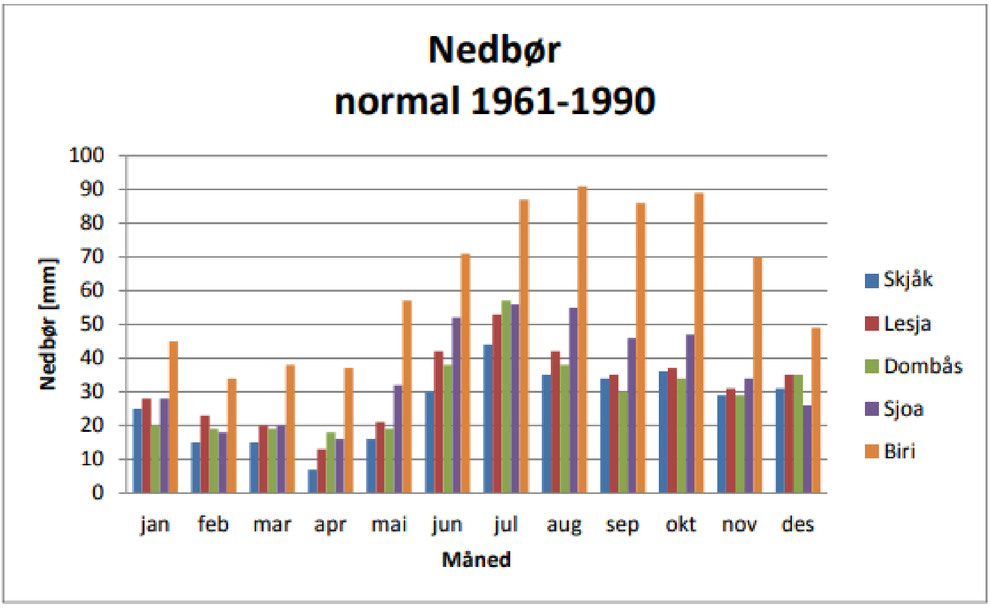

Figure 4.6: *Monthly average precipitation measured in the period 1961-1990 for five meterological stations in Gudbrandsdalen. Data from eklima.no (Credit: Walberg and Devoli (2014)).*

Predicted future climate conditions

As mentioned in the Introduction, it is well documented that temperatures as well as rainfall intensities and frequencies have increased in Norway over the last fifty years, and that the trends are expected to persist in the future (St.mld. 33, NGI (2013)). In St.mld. 33 ”Climate Change in Norway” many results of future climate predictions for Norway are summarized. Calculations show that precipitation can increase by between 5 and 30 % across the country, and projections indicate that there will be more intense precipitation in most areas. Since Kvam is a cold and dry inland area, the trends are not expected to be as significant here as in wet regions in Norway like the south west coast (NGI (2013)). Still, studies show that increased snowfall and precipitation can be expected also in Gudbrandsdalen in the future.

As part of a probabilistic rainfall-induced landslide study in Otta (located 15km north of Kvam), daily local precipitation values for different return periods under present conditions and future climate scenarios were found (Melchiorre and Frattini (2012)). The climate scenarios were provided by the GeoExtreme project (NGU (2009), Jaedicke et al. (2008)), where a dynamic

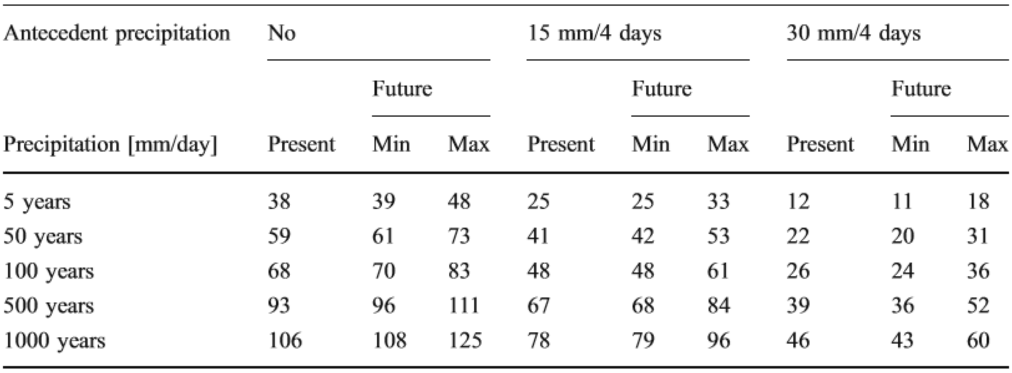

Antecedent precipitation	No			15 mm/4 days			30 mm/4 days		
		Future			Future			Future	
Precipitation [mm/day]	Present	Min	Max	Present	Min	Max	Present	Min	Max
5 years	38	39	48	25	25	33	12	11	18
50 years	59	61	73	41	42	53	22	20	31
100 years	68	70	83	48	48	61	26	24	36
500 years	93	96	111	67	68	84	39	36	52
1000 years	106	108	125	78	79	96	46	43	60

Figure 4.7: *Calculated values of precipitations for different antecedent precipitation conditions and for different return periods (Melchiorre and Frattini (2012)).*

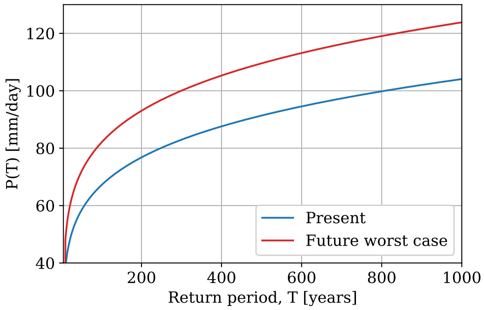

Figure 4.8: *Rainfall intensities, I_z, evaluated for present conditions and the worst future scenario presented by (Melchiorre and Frattini (2012)).*

regional climate modelling approach was used. In this approach, several global and regional models (300km to 50km resolution) are down-scaled and bias-corrected according to historical precipitation records from a rain gauge in Otta. Daily extreme precipitation events with return periods longer than 5 years were found using the following semi-empirical equation, calibrated for Norwegian data (Førland and Kristoffersen (1989)):

$$P(T) = P(5)exp(\lambda(\ln(T - 0,5) - 1,5)) \tag{4.1}$$

where $\lambda = 0,3584 - 0,0473\ln(P(5))$ for $25 < P(5) \leq 200$. The resulting present, and best and worst case future scenario values of 24 hour long constant rainfall intensity, for different

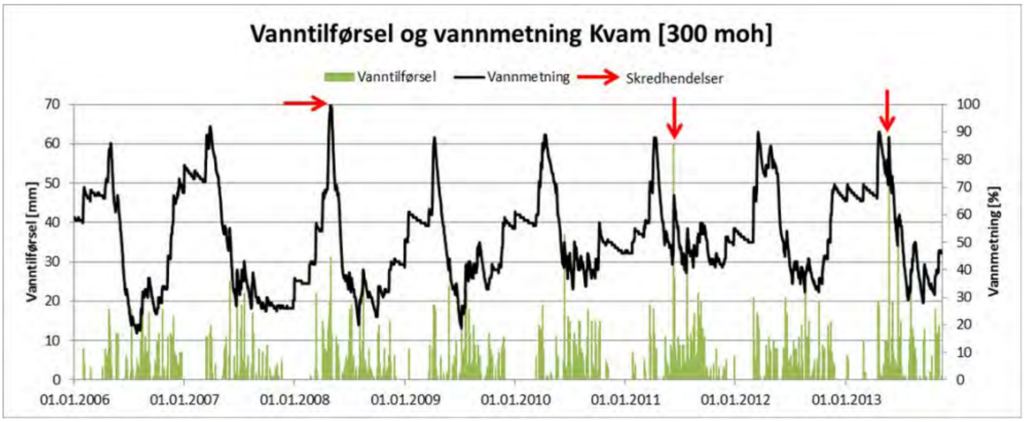

Figure 4.9: *Simulated ground saturation (black line) and precipitation (green histogram) interpolated at Kvam 300 MAMSL over a six year period with observed landslide activity(Walberg and Devoli (2014)).*

antecedent precipitation conditions and return periods, can be studied in Figure 4.7.

In this Kvam case study, the present and future worst case scenario rainfall events with return periods $T = 50, 100, 500$ and 1000 from 4.7 are selected. Antecedent precipitation is not modeled explicitly. Figure 4.8 shows the relationship between return period and 24 hour rainfall intensity for these two scenarios (as calculated by Equation (4.1)).

4.2.3 Characteristics of the 2011 landslides

In Figure 4.9 the 2011 landsliding time of occurrence is marked by the middle red arrow. Figure 4.9 shows that at the time of failure, the ground saturation was considerable, but not at its peak value that spring. The measured precipitation values prior to the event are very high. With a measured value close to 60 mm on the 10th of June, this 24-hour precipitation alone was more that what is average for June in total (Ref. Figure 4.6). Figure 4.10 shows hourly average rainfall interpolated to Kvam, calculated from available 1-h rainfall maps (www.xgeo.no) for both the 2011 and 2013 events (Schiliro and Cepeda (2016)). In NVE's analysis of the 2011 and 2013 landslides, it is concluded that the heavy local precipitation following snow melting was the triggering cause of the slides and debris flows.

Characterization of the landslides in Kvam in terms of size and shape has been done based on high resolution DEM's and by field surveys. As part of their master thesises, Holm (2012) and

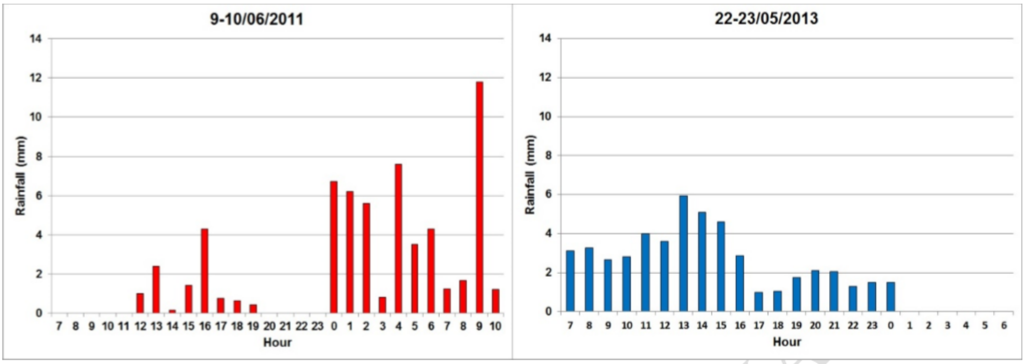

Figure 4.10: *Hourly average rainfall interpolated to Kvam, calculated from 1-h rainfall maps (www.xgeo.no) for the 2011 (left) and 2013 (right) rainfall events (Schiliro and Cepeda (2016)).*

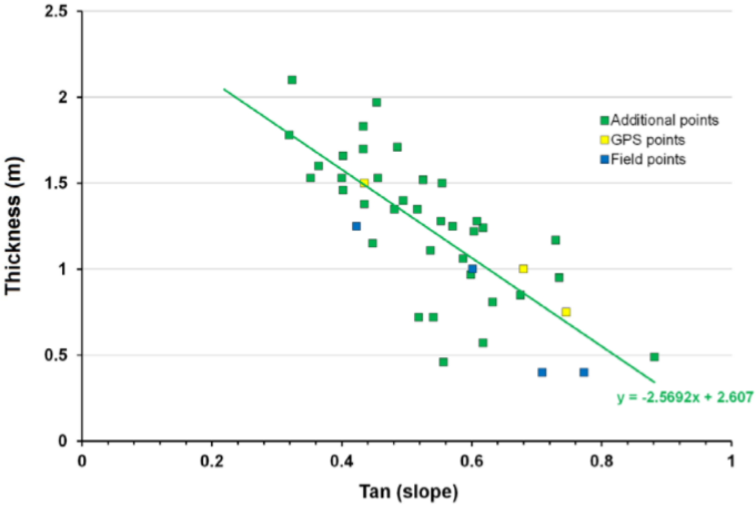

Figure 4.11: *Soil thickness model for landslides observed at Kvam: a linear relationship between soil thickness and slope angle derived with three different types of thickness data. GPS-points by Holm (2012), Field points by Edvardsen (2013) and DEM points by Schiliro and Cepeda (2016).*

Edvardsen (2013) completed field observations of the source areas and slide paths of the Kvam landslides. Photos of the failures, together with descriptions of slope angles, depths of failure surfaces and soil materials are available in their reports. Based on their data and data calculated from high-resolution DEM's, Schiliro and Cepeda (2016) derived a linear relationship between slope thickness and tangent of the slope angle in the Kvam landslides. Figure 4.11 shows the data points and soil thickness model. Most of the reported failure slope angles are between 20 and 35 degrees. Reported soil thickness values range from 0,4 to just above 2 m.

Photos of two landslides in Kvam taken during the summer in 2011 are shown in Figure 4.12 on the next page. The top left photo shows a 11 m wide and 0.70 m deep triggering zone with a slope angle of 30 degrees. The sediments are described as loosely packed and unsorted, and soil thickness of the slide varied between 1 and 1.5 m. The slide was triggered in a clear-felled area, and shear strength reduction due to deterioration of tree roots is considered an important cause of sliding (Edvardsen (2013)). The bottom photos show a typical slide triggered in a forested area in Veikledalen, where dozens of slides were observed after the 2011 event. Here, the slide soil thickness was measured to a shallow 40 cm and the slope angle to 40 degrees. Again unsorted till materials, with presence of larger blocks are observed.

Based on their field surveys, Holm (2012) and Edvardsen (2013) concluded that multiple triggering mechanisms have been possible at Kvam in 2011. Shallow sliding of saturated or near-saturated soil masses is assumed to be a main mechanism, as is assumed for the slides shown in 4.12. As discussed in chapter 2, this is the mechanism that the implemented stability models in this study are aiming to describe.

Figure 4.12: *Top photos: Slide triggered on a clear-felled area south of the river in Kvam. Left: Triggering zone. Right: Same landslide seen from below. Blue arrow indicates the triggering zone and red arrow points to exposed bedrock in the slide path. Bottom photos: Slide triggered in forested hill side of Veikledalen. Left: Trigger zone. Right: Same slide path seen standing in the triggering zone. Photos by: Edvardsen (2013), included with permission.*

4.3 Case study parameter estimates

This section provides an overview of the selected values for the parameters used in the prediction models to simulate the occurrence of rainfall-induced landslides in the Kvam case study. A probabilistic approach is adopted to describe the available knowledge about the model parameters. The probabilistic approach is considered suitable for this study as it provides a basis to describe uncertainties associated with these parameters. Uncertainties associated with the parameters of the case study arise from the lack of knowledge (e.g., lack of field and laboratory investigations) and the inherent natural variability (e.g., spatial variability of soil moisture contents and soil properties).

Table 4.1: *Uncertain model parameters for the Kvam case study.* Probability distributions: U = uniform, LN = lognormal, N = normal, MN = multivariate normal, G = Gumbel. Distribution parameters: μ - mean, σ - standard deviation, CoV - coefficient of variation, Σ - covariance. References: [1] Schiliro and Cepeda (2016), [2] Melchiorre and Frattini (2012), [3] Lacasse and Nadim (1997), [4] Guan and Fredlund (1997), [5] division NTNU (2015), [6] Lars Lundin (1990b), [7] Jørgensen (1977), [8] Førland and Kristoffersen (1989), [9] Duncan and Wright (1980).

Parameter	**Symbol**	**PDF**	**Model parameters**	**Ref.**
Slope angle	θ [°]	U	$\theta_{min} = 20.0 \quad \theta_{max} = 36.0$	[1]
Soil depth	H [m]	LN	$\mu = 2.569 \cdot \tan(\theta) + 2.607$ $\sigma = 0.271$	[1]
GW-table depth	H_w [m]	U	$H_{w,min} = 0 \quad H_{w,max} = H$	-
Effective cohesion	c' [kPa]	LN	$\mu = 4 \quad CoV = 0.3$	[2],[3]
Friction angle	ϕ [°]	N	$\mu = 32 \quad CoV = 0.1$	[2]
Soil specific gravity	G_s [-]	N	$\mu = 2.7 \quad CoV = 0.054$	[4],[5]
Void ratio	e [-]	N	$\mu = 0.25 \quad CoV = 0.025$	[5]
Sat. permeability	k_{sat} [m/s]	LN	$\mu = 5 \cdot 10^{-6} \quad CoV = 0,5$	[2],[5],[6]
Diffusivity	D_0 [m^2/s]	LN	$\mu = 5 \cdot 10^{-4} \quad CoV = 0.25$	[2]
Grain size ratios	α [-]	MN	$\alpha = [\alpha_{clay}, \alpha_{silt}, \alpha_{sand}]$ $\mu_\alpha = [0.2 \quad 0.35]^T$ $\Sigma_\alpha *$	[5],[7]
Rainfall intensity	I_z [mm/day]	G	Equation (4.1)	[2],[8]
Model error	ε [-]	N	$\mu = 0.0 \quad \sigma = 0.05$	[9]

$\Sigma_\alpha *$ is the covariance matrix of the grain size ratios given by:

$$\Sigma_\alpha = \begin{bmatrix} 0.0019 & -0.0008 \\ -0.0008 & 0.0027 \end{bmatrix}$$

Uncertainties associated with a range of geotechnical, hydrological, climate and modelling parameters are presented in Table 4.1 and described by assigning probability distributions to the parameters. The selection of the probability distribution parameters in Table 4.1 aims to reflect the geotechnical, hydrological and climate properties associated with landslide events occurring in till deposits in the Kvam area hillsides, as described in the preceding sections. As extensive field investigation data are not available for the Kvam site, the selection of probability distribution functions and parameters cannot be validated empirically. The probability distributions are instead chosen based on representative values reported in a number of sources, as reported in Table 4.1. Recommendations for distribution functions are given by Lacasse and Nadim (1997).

Most of the parameters in Table 4.1 are considered mutually independent. However, a positive correlation between c and ϕ is assumed with the correlation coefficient of $\rho_{\ln c - \phi} = 0,5$ (Melchiorre and Frattini (2012)). Similarly, a positive correlation is assumed between k_{sat} and D_0 with the correlation coefficient of $\rho_{\ln k_{sat} - \ln D_0} = 0,5$, because both parameters are measures of how easily water flows through the pores of the soil (Ref. Section 2.2.4). A linear regression is assumed between the tangent of the slope angle and the soil thickness, as shown in Figure 4.11, page 54.

The values of the slope angle is modelled as a uniformly distributed pseudo-random variable, to examine the effects of Bayesian updating over the range of possible slope angles encountered in the field. In their sensitivity study of uncertainties in rainfall-induced landslide prediction, using Iversons infiltration model and a infinite slope stability model, Melchiorre and Frattini (2012) found that slope angle influenced factor of safety estimates the most. It is therefore of interest to observe interactions of this variable with the others in the model.

GW-table is also modelled as a uniformly distributed variable, in order to describe the significant spatial variation typically observed in the field (Lars Lundin (1990b), Ref. Section 2.1).

4.4 Case study approach

The aim of this case study is to analyze the landslide events that occurred in Kvam in 2011 and generate additional insights on the parameters controlling the occurrence of rainfall-induced landslides. Such learning process will be facilitated by adopting the Bayesian updating framework. The Bayesian updating framework is implemented with two types of landslide prediction models to investigate the effects of model complexity on the updating process: the analytical and the numerical models, as presented in Chapter 2. The evaluation of the effects of model complexity on the updating process is important due to relatively high computational demands commonly associated with Bayesian updating algorithms that require numerous repeated evaluations of prediction models (Ref. Chapter 3). The effects of the implementation of the analytical model on the updating process will be examined by comparing the results with the ones obtained with the more advanced numerical model.

In the context of the Kvam case study, Bayesian updating will be employed to update knowledge on the uncertain model parameters in Table 4.1 (i.e., prior knowledge) with the observation of slope survival of the rainfall event in 2011 at Kvam. The results of the updating is posterior knowledge, which combines the prior information and the additional information provided by the observation. The additional information provided by the observation often provides a basis to reduce uncertainties in the prior knowledge. Reducing the uncertainties provides a basis to increase the knowledge on the uncertain parameters, identify the most influential parameters controlling the occurrence of rainfall-induced landslides, and improve the capacity of prediction models to provide more accurate and robust landslide predictions for future uncertain rainfall events.

The effects of model complexity on reducing the uncertainties in the model parameters and identifying the most influential parameters controlling the occurrence of rainfall-induced landslides will be examined by conducting three sub-studies: (a) Bayesian updating with the analytical model and (b) Bayesian updating with the numerical model. The effects of updating on improving the predictive capacity for future uncertain rainfall events under varying climate scenarios is examined in the last sub-study (c) Landslide predictions under varying future climate scenarios. Implementation details for these sub-studies are presented in the following sections.

(a) Bayesian updating with the analytical model

The prior knowledge is defined by the following nine random parameters that are required by the analytical stability and infiltration models: $\mathbf{X} = [\theta, c', \phi', G_s, e, k_{sat}, D_0, H, H_w, \epsilon]$. The probability distributions and distribution parameter values are according to Table 4.1. Note that θ as a pseudo-random variable and ϵ as a model error are not being updated.

The implemented Bayesian updating algorithm is based on the Subset Simulation method (Ref. Chapter 3), which is implemented in a Python code. The Subset Simulation method is implemented with $n = 20000$ simulations per iteration. Recall the flowchart in Figure 3.2 page 43. The initial set of $n_{MC} = 20000$ samples of random parameters are generated with direct Monte Carlo method. The Subset Simulation method is implemented in the standard normal space, with the samples converted to the input space for the purpose of model analysis. For each set of random variable realization, $\mathbf{x} \in \Omega_x$, the stability of the slope is evaluated by calculating the slope factor of safety prior to and after the rainfall event at Kvam in 2011. The values of F_s prior and after the rainfall are calculated across 100 points over the slope depth, Z, with the analytical infinite slope stability model (2.16). After $F_s(\mathbf{x}, t = 0, Z)$ is found, the analytical rainfall infiltration analysis described in Section 2.2.4 is evaluated for each set of random variable realizations. A constant rainfall with the intensity of 60 mm/day is applied, corresponding to the total $T = 24$ hour rainfall measured at Kvam 09-10.06.2011. The factor of safety at the end of the infiltration analysis, $F_s(\mathbf{x}, t = T, Z)$, is then evaluated using the same equation (2.16). The modelling error ε in 4.1 is added to the $F_{s,}$ estimates. Lastly, the final critical value of factors of safety, prior to and after the rainfall event are found as the minimum value across the soil depth, $F_s = \min(F_s(Z))$. The observation of slope survival of the rainfall event is integrated in the following performance function:

$$g(\mathbf{x}) = \max(1 - F_s(\mathbf{x}, t = 0), 1 - F_s(\mathbf{x}, t = T)) \tag{4.2}$$

where $g(\mathbf{x})$ is the performance function. Equation (4.2) is formulated such that $g(\mathbf{x}) < 0$ for a slope that is stable before and stable after the rainfall, thus corresponding to the slope surviving the rainfall event. Otherwise, in the case that the slope is unstable prior to the rainfall and/or after the rainfall, the performance function takes the value $g(\mathbf{x}) \geq 0$.

The conditional subsets of the iterative process in the Subset Simulation method are defined with the conditional probability of $p_0 = 0.1$. This means that in each iteration of the Subset Simulation algorithm 2000 samples from a given iteration with the lowest value of the performance function are transferred to the next iteration. The iterations proceed until at least 2000 of the samples with the lowest value of the performance function satisfy the limit state condition $g(\mathbf{x}) < 0$. After the limit state is reached, sampling from the posterior parameter distributions is performed with $n = 20000$ samples per iteration. These randomly realized samples then correspond to the samples from the posterior distributions. Lastly, the posterior $F_s(\mathbf{x}, t = 0)$ and $F_s(\mathbf{x}, t = T)$ estimates are evaluated with these posterior samples and the same analytical equation (2.16).

(b) Bayesian updating with the numerical model

In this study the Bayesian updating algorithm based on the subset simulation method (Ref. 3.3.2) is implemented. The difference between study (a) and this one is that the prior and posterior, initial and post-rainfall, values of F_s are evaluated using the numerical Plaxis infiltration and stability models presented in sections 2.2.5 and 2.3.3. Pore pressure profiles developing due to rainfall infiltration is calculated in the two flow phases described on page 28, and initial and post-rainfall stability is evaluated with the three phases described on page 29. Modelling error is excluded from calculation.

The sequential coupling between the transient infiltration and slope stability models is executed in a Phyton code that communicates with Plaxis. The Phyton program code establishes the slope model geometry and defines the model variables in Plaxis according to the random realizations in the MCS. Infiltration and stability phase calculations are executed in Plaxis and results are saved by the Phyton code.

Seven parameters of the numerical stability and infiltration models are modelled as random variables: $\mathbf{X} = [\theta, c', \phi', G_s, e, k_{sat}, \alpha, H, H_w]$. Slope angle is modeled as a pseudo random variable with discrete outcomes $\theta = [20°, 25°, 30°]$, to simplify the implementation of the numerical model. The input probability distributions and distribution parameter values are again according to Table 4.1. A 24 hour long rainfall is applied in transient the infiltration analysis, equal to the interpolated hourly rainfall at Kvam 09-10.06.2011 presented in 4.10.

Otherwise, the Bayesian updating algorithm and subset simulation processes are the same in this study as in study (a). Recall the again the flowchart in Figure 3.2 page 43, and the subset simulation process described in the preceding Chapter 3 with the performance function (4.2). Since this sequentially coupled numerical infiltration and stability analysis is considerably more computationally demanding than the analytical analysis, only $n = 500$ initial simulations are evaluated per iteration. The conditional subsets of the iterative process in the Subset Simulation method are defined with the conditional probability of $p_0 = 0.1$. After the limit state is reached, sampling from the posterior parameter distributions is performed with $n_{MC} = 1000$ samples per subset simulation iteration.

(c) Landslide predictions under varying climate scenarios

This third sub-study investigates the effects of Bayesian updating on improving the predictive capacity for future uncertain rainfall events under varying climate scenarios. In addition to demonstrating how the Bayesian updating framework can be used in landslide prediction, the study aims to investigate the effects of climate change on slope stability. A simple approach is chosen, using the analytical rainfall infiltration and stability models and prior and posterior results from the study (a).

Recall the simple direct MCS Bayesian updating approach presented in Section 3.3.2. The effects of updating on the estimated failure probabilities are evaluated by calculating the failure probabilities based on the prior and posterior knowledge (Ref. (3.12). The prior knowledge is the $n = 20000$ sets of direct MCS parameter realizations realized in the first part of study (a). The posterior knowledge is the $n = 20000$ sets of parameter values sampled from the posterior distributions after updating in study (a).

The uncertain future rainfall events considered in this study are modeled in terms of intensities of different return periods. The present and future worst case scenario rainfall events with return periods $T = 50, 100, 500$ and 1000 from 4.7 are selected. Antecedent precipitation is not modeled explicitly. Figure 4.8 shows the relationship between return period and 24 hour rainfall intensity for these two scenarios (as calculated by Equation (4.1)).

4.5 Results and discussion

The results of the Kvam case study are presented in the following sections. The presentation of the results is organized in terms of the three sub-studies, as introduced earlier. Discussions regarding the effect of updating on the uncertain parameters of the models and stability predictions are given.

The sample mean values and sample 95% confidence bounds of the prior and posterior parameter are estimated with the Nadaraya-Watson non-parametric regression model. Regression curves illustrate system responses to sets of input parameters, and non-parameteric regression is flexible in regards to the regression curve shape (e.g. Baecher and Christian (2003)). This makes it possible to illustrate variations in parameter sample means and confidence bounds over the range of slope angles. Details of the Nadaraya-Watson non-parametric regression model is available in literature, e.g. Wasserman (2006). The values of the 95% confidence bounds correspond to the range of output values that 95% of the samples are located within.

The effects of the updating on the parameter PDF's are examined by plotting prior and posterior parameter distributions using the following function from the SciPy extension in Phyton: `scipy.stats.gaussian_kde`. This is a non-parametric way of estimating PDF's by smoothing histograms with automatic bandwith determination (docs.scipy.org).

In terms of computational efficiency, the analytical model proves to perform significantly better than the numerical, as expected. The average computational time per single rainfall infiltration and slope stability simulation in the numerical model is 5-6 minutes In contrast, evaluation and updating of 100 samples sets takes under 5 seconds with the analytical models. In both the numerical and analytical models, the probabilities of slope survival are shown to be high for the considered parameter uncertainty ranges. Thus, multiple iterations of subset simulation is not needed for high accuracy in results.

4.5.1 (a) Bayesian updating with the analytical model

Results

In figure 4.13, 20000 samples of posterior slope factors of safety after Bayesian updating with the analytical models are presented. Calculated prior and posterior mean values and 95% confidence bounds are shown. The left figure (a) shows the results prior to the rainfall event, while the right figure (b) shows results after rainfall infiltration. Each blue dot correspond to a calculated posterior $F_{s,i}$ for a given set of posterior parameter realizations $\mathbf{x}_i$.

Figures 4.14 to 4.16 in the following pages present the results of the Bayesian updating for the uncertain parameters of the analytical slope stability and rainfall infiltration models. The parameter distributions are updated according to the observation of a stable slope before and after the 2011 rainfall event in Kvam. The pictures show 5000 samples of the total realized from the posterior distribution, with calculated prior and posterior mean values and 95% confidence bounds. Figures 4.16 (a) to 4.16 (f) show the updated PDF's for 20000 samples of these given deterministic slope angle values: $\theta = 20°, 25°, 30°$ and $35°$. Here, parameters that are significantly affected by updating are shown only.

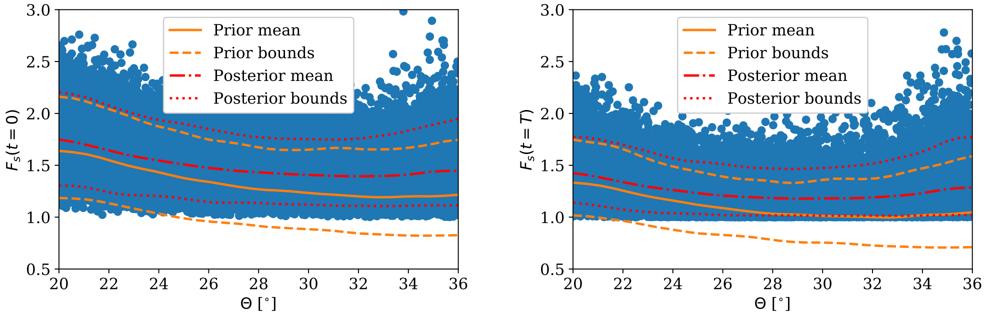

(a) **(b)**

Figure 4.13: *Analytical model: Factors of safety with respect to slope angle: (a) Initial,* $F_s(t=0)$ *(b) At the end of 2011 Kvam rainfall event,* $F_s(t=T)$.

Discussion

Factors of Safety

Comparison of 4.13 (a) to (b) illustrate that the analytical infiltration model is able to capture the negative effect of rainfall infiltration on slope stability that has been observed at Kvam. The prior and posterior F_s mean and confidence bound values decrease between $t = 0$ and $t = T$ for all slope angles. Also, not surprisingly considering that the updating information event is one of slope survival, the posterior F_s estimates are lower than the prior.

The effect of Bayesian updating on uncertainty mitigation in factor of safety prediction is visible in Figures 4.13 (a) and (b). After samples disagreeing with the stability observations are removed, the confidence bounds tighten. The reduction in F_s uncertainty after rainfall infiltration will be large for those slope angle ranges with low ratios of prior realized stable to unstable F_s values. In the results, the 95% confidence range is reduced the most for slopes with θ just below and around ϕ.

The rate of increase of the F_s mean and confidence bounds increases with the value of θ. This observation indicates the effect of the information strength on the updating process. In terms of the Bayesian updating framework, the constraint on the model output outcome space imposed by the slope survival information is strongest for the most critical slopes. Likewise, the constraint imposed by updating on the parameter sample outcome spaces $\Omega_{\mathbf{x}}$ is the strongest on parameter outcomes that are the most critical for slope stability. This also implies that for the low slope angles where few of the prior randomly realized sample sets make up unstable slopes, updating will have less effect on the parameter distributions.

An important finding in the results is the slight positive correlation between slope steepness and stability observed for high slope angles visible in figures 4.13 (a) and (b). On the lower θ range, the prior and posterior mean and confidence bounds suggests that increased slope angle has a negative effect on initial slope stability. However, around $\theta = 32°$ this trend ceases, and the posterior mean values even increase. This is likely to be associated with relatively low values of soil thickness for higher values of θ, as predicted by the prior linear model (Ref. 4.11 page 54). Low slope thickness is stabilizing both in terms of the decrease in stress on the slip surface by $H\gamma_s$ itself, and in terms of the limiting bound it puts on positive pore pressure build-up.

Model parameters

Considering Figures 4.14 to 4.16, it can be concluded that updating based on the observation of slope survival of the Kvam rainfall event has the most significant effect on parameters H, H_w, c and ϕ in the analytical model. The effect, in terms of reducing uncertainty, is biggest for parameters H and H_w, at high slope angles, and for phi. This is inferred from comparison of the prior confidence ranges with the narrowed posterior confidence ranges. It should be noted that the differences between prior and posterior distributions for different θ values can be larger in Figure 4.16 than in Figure 4.14 because the regression analysis in the Figure 4.14 results smooths over local variations.

Reducing uncertainties, in terms of reduced variance in probability distributions, is not the only motivation for doing Bayesian updating. Increased knowledge on the relative importance of

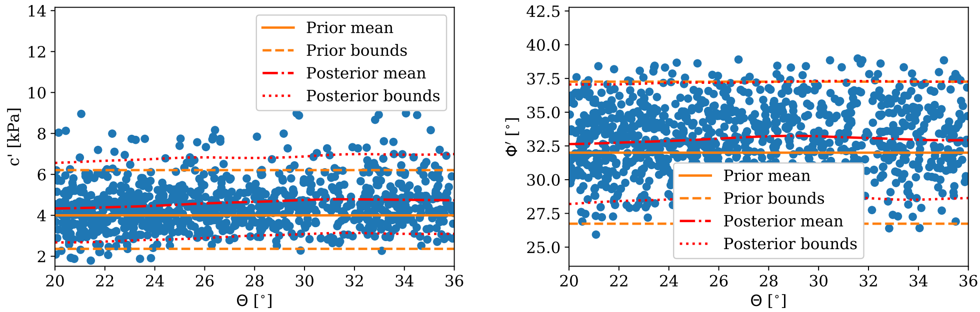

(a) Effective cohesion **(b)** Friction angle

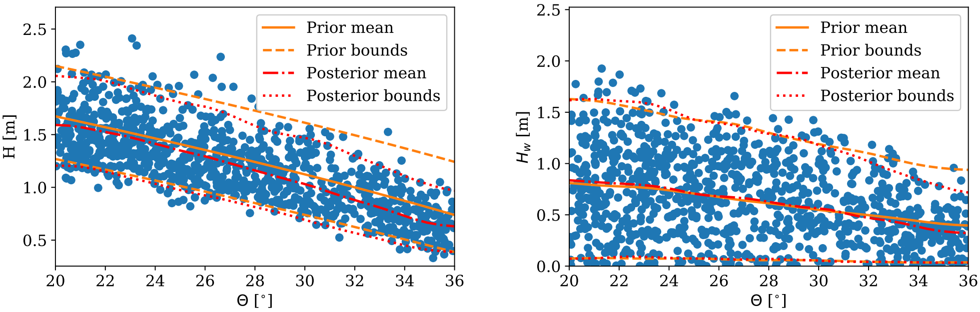

(c) Soil thickness **(d)** GW-table depth

Figure 4.14: *Samples from posterior parameter distributions with prior and posterior means and 95% confidence interval bounds.*

different model variables on slope stability can be gained from comparison of prior and posterior parameter sample distributions.

One of the main findings in the results is the increased likelihood of low slope thickness, H, for high slope angles in the posterior distributions. This can be observed in Figures 4.14 (c) and 4.16 (c). Figure 4.16 (c) shows particularly well how the updating effects on the slope thickness PDF, in terms of lowered mean value estimate, is biggest for the slope with $\theta = 35°$.

Posterior samples of H_w, depth of the initial GW-table level, are presented in Figure 4.14 (d). In 4.16 (d) the posterior distribution is plotted in values of GW-table height, $H - H_w$. Comparison with the prior distributions reveal that samples of high GW-table levels are discarded in the high slope angle range in the updating process. This observation indicates that the prior-to-rainfall

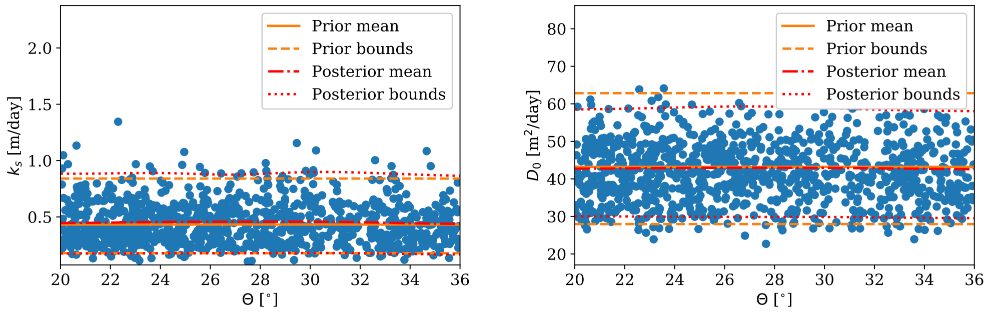

(a) Permeability **(b)** Diffusivity

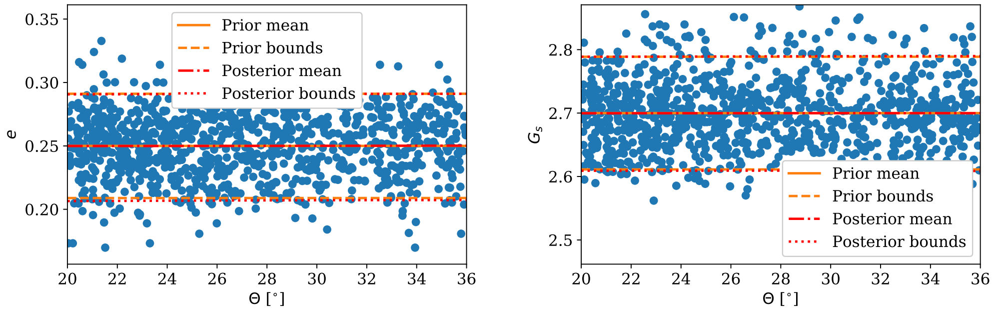

(c) Void ratio **(d)** Soil specific gravity

Figure 4.15: *Samples from posterior parameter distributions with prior and posterior means and 95% confidence interval bounds.*

moisture content is an important controlling factor of slope stability in rainfall-induced landslides on steep slopes.

The results discussed above suggest that the combination of high soil thickness and high initial GW-tables is critical for rainfall-induced slope stability at high slope angles. This is in good agreement with literature (Zhang et al. (2011), Rahardjo and Leong (2007), Melchiorre and Frattini (2012)). The observed importance of $H - H_w$ is consistent with previous evaluations of the Kvam 2011 landslide event, which concluded that high moisture contents (due to snow melt) in combination with rainfall was the triggering cause of the slides and debris flows (Walberg and Devoli (2014), Edvardsen (2013)).

The low observed effect of updating on these critical parameters (H and H_w) in gentle slopes can be attributed to the discussed low strength of the updating information on these generally stable and rainfall-insensitive slopes.

The effects of updating on uncertainties in strength parameters c' and ϕ' are shown in Figures 4.14 (a) and (b), and in 4.16 (a) and (b). The plots suggests that slopes which are stable trough the rainfall are more likely to be associated with high values of effective cohesion and friction angles than the prior model slopes. The increased likelihood of higher values is generally low: the mean value shifts are less than the input standard deviation values. In contrast to the observed effect on parameters H and H_w, the effect of updating on c' and ϕ' is close to constant over the whole slope angle range, implying that low values of these parameters are equally critical for all slopes.

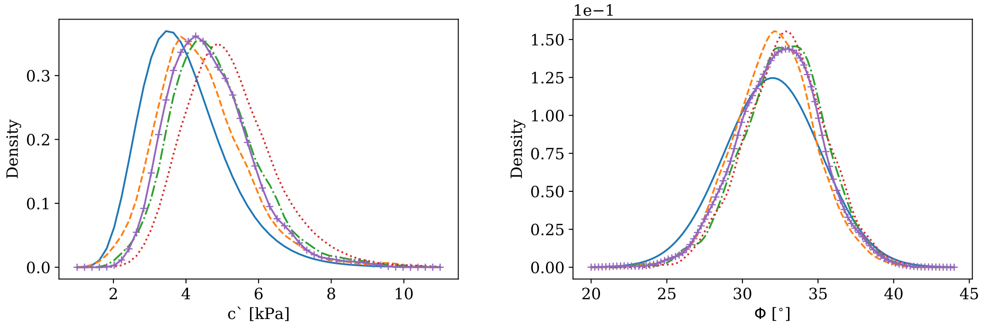

(a) Effective cohesion **(b)** Friction angle

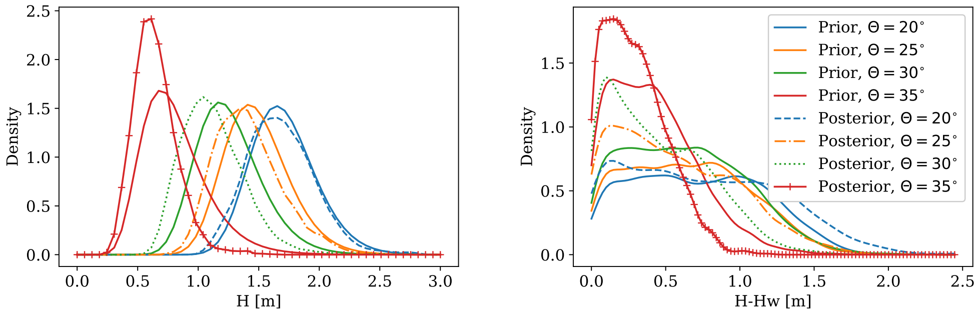

(c) Soil thickness **(d)** GW-table height

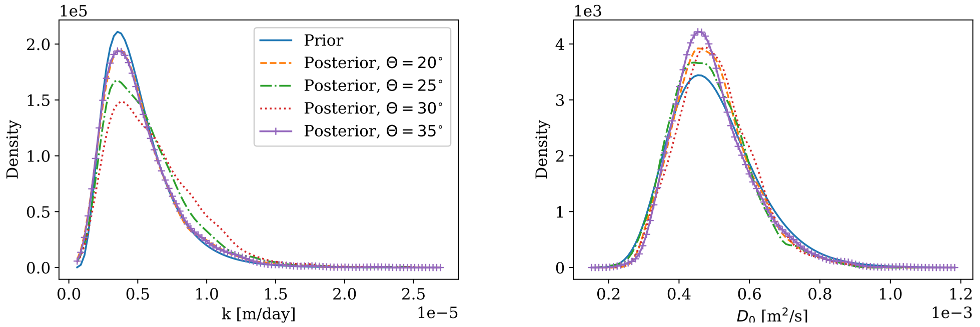

(e) Permeability **(f)** Diffusivity

Figure 4.16: *Prior and posterior PDF's calculated with the analytical model.*

Another finding is that variation of the hydraulic properties within the ranges considered in this study seems to have little influence on stability. Thus, indicating that unsaturated behaviour of the soil does not play a critical role in the analytical landslide prediction model. This observation is important because these variables are associated with high uncertainty and spatial variability in the field, and they are generally difficult to measure (Lars Lundin (1990a), Fredlund (2012)). Figures 4.15 (a) and (b), and 4.16 (e) and (f) present the effect of updating on parameters k_s and D_0. The observed influence of slope survival information on sampling of these variables in 4.15 (a) and (b) is near constant and low over the full slope angle range. Furthermore, depth to GW-table, H_w, which is a controlling parameter of the time needed to saturate the soil above GW-table, is also seemingly unaffected after updating (with the exemption of steep slopes). Similar results were obtained by Melchiorre and Frattini (2012) in their sensitivity study of the same analytical rainfall-induced slope stability models. They suggested that the findings could be explained by the upper boundary of pressure head, the beta-line correction (Iverson (2000)). They argued that potentially extremely large variations of pressure head resulting from large variations in k_{sat} and D_0 are hampered by this beta-line correction. However, such potentially extremely large pore pressures are not realistic (Tsai and Yang (2006)).

As stressed in section 2.2.4, although Iversons analytical model is popular and frequently implemented in rainfall-induced landslide predictions, it is insufficient in describing the true complex physical behaviour of infiltration. A consequence of this is that the results of varying the model input parameters randomly can be counter intuitive. Recall Equation (2.9a) on page 16, for constant values of I_z and D_0, an increase in k_s will lower the impact of infiltration on the developing pore pressures. This effect might be the reason for the very subtle increase in mean k_s in 4.15 (a) after updating.

Lastly, in Figures 4.15 (b) and (c), the distributions of e and Gs are left practically unchanged after updating, which indicates that variation in these parameter within the given input ranges has little influence on slope stability.

4.5.2 (b) Bayesian updating with the numerical model

Results

The posterior initial and post-rainfall infiltration F_s distributions calculated with the numerical stability and rainfall infiltration models are shown in Figure 4.17. Due to the automatic smoothing bandwidth of the density function, it looks like some of the posterior F_s realizations have values below 1. This is not the case. It should be mentioned that some high F_s value outliers not visible in 4.17 were also observed. They may be explained by numerical instabilities, but this is not investigated in detail.

The prior and posterior PDF's of the uncertain parameters of the numerical models are shown in Figure 4.18. The following slope angles are considered: $\theta = 20°, 25°$ and $30°$. Calculation is done based on 1000 samples from the posterior distributions only, due to mentioned high computational demands associated with the numerical models.

Discussion

Factors of Safety

Figure 4.17 shows that, similarly to the analytical model, the numerical model captures the negative effect of the Kvam rainfall on average slope stability. The analytical and numerical factors of safety are largely in the same range.

Model parameters

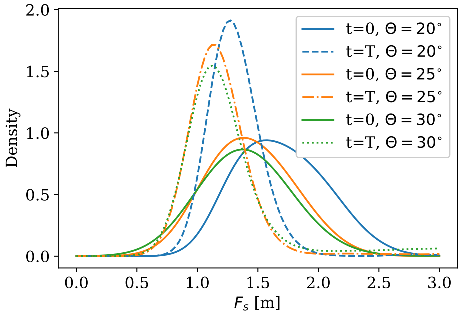

Figure 4.17: *Numerical model: Posterior factors of safety with respect to slope angle: (a) Initial, $F_s(t = 0)$ (b) At the end of 2011 Kvam rainfall event, $F_s(t = T)$.*

The results of the updating process on the parameters of the numerical model, shown in Figures 4.18 and 4.19, share many of the trends observed in the analytical results. Analogous to the analytical results, the PDFs of parameters c' and H are visibly influenced by updating. The trend of increasing updating effect on parameter distributions with increasing slope angle is observed in these results also. Also consistent with analytical results, the information of slope stability does not seem to influence uncertainties associated with e, G_s and k_{sat}. Due to the low number of samples and exclusion of model uncertainty in the stability estimates, larger variation in the plotted distributions is expected here than in the analytical results.

A difference between the numerical and analytical results is the less observed influence of updating on GW-table height $H - H_w$ in 4.18 (d). Comparison of the distribution shapes and the density-range on the y-axis to the analytical equivalents in 4.16 (d) (neglecting the $\theta = 35°$ result), reveal that high $H - H_w$ values are slightly less likely after updating in the numerical

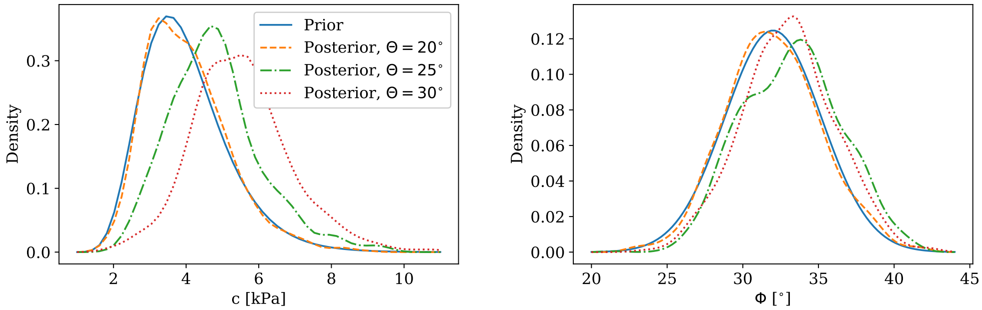

(a) Effective cohesion **(b)** Friction angle

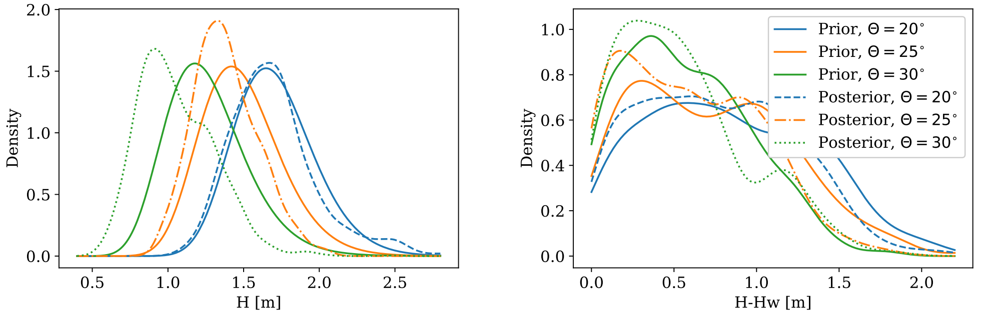

(c) Soil thickness **(d)** GW-table height

Figure 4.18: *Prior and posterior PDS's calculated with the numerical model.*

model than in the analytical. This may be due to the low number of posterior samples in the numerical model. More simulations would have to be run to properly investigate the effect of initial moisture content on stability in the numerical model.

The effects of updating on strength parameters c' and ϕ' are presented in 4.18 (a) and (b). For steeper slope angles, rightward shifts of the cohesion probability densities increase. For the 30° slope, almost all samples with cohesion less than the input mean, $\mu_c = 4$, are disregarded. The effect of updating on steep slope angles is slightly bigger than in the analytical results. One of the main reasons for this difference may be the exclusion of model uncertainty. Only a subtle effect of updating can be observed in posterior ϕ' samples for steep slopes in 4.18 (b).

In Figure 4.18 (c), the effects of updating on uncertainties in slope thickness are illustrated. As in the analytical model, for high θ values, samples with the highest H values are less likely after updating. The shift in the distributions towards low slope thickness is more significant here

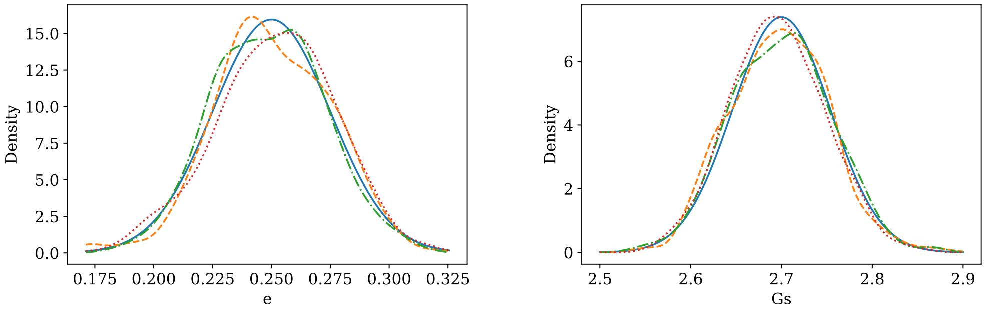

(a) Void ratio

(b) Soil specific gravity

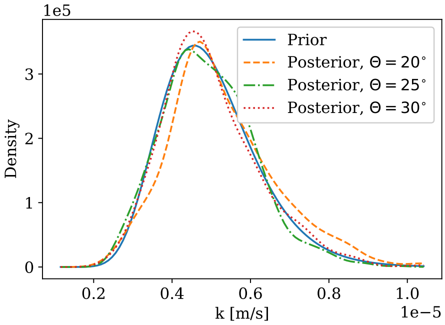

(c) Permeability

Figure 4.19: *Prior and posterior PDS's calculated with the numerical model.*

than in the analytical analysis. Again, exclusion of model uncertainty may be the main reason for this inconstancy.

Lastly, low impact of updating on parameters controlling unsaturated flow is observed in the numerical model as in the analytical. Figures 4.19 (a) to (c) show that the differences between prior and posterior e, G_s and k_{sat} distributions are insignificant, considering the expected variation due to low number of samples. Recall that the F_s results in Figure 4.17 implies that rainfall infiltration has a visible negative impact on slope stability in the numerical model. Still, the low updating effect on hydraulic parameters suggests that the effect of rainfall infiltration on slope stability depends little on variation of the hydraulic parameters within the ranges considered in this study and for the considered rainfall intensity and analysis duration. These results could be attributed to the relatively low influence of these parameters to the observation event in this study. The updating information is defined only by factors of safety before and after the rainfall event. Thus, the effects of the transient rainfall infiltration controlled by these parameters may not have been captured within the observation event. One explanation could be that the process is mainly completed before the end of rainfall. In other words, that the rainfall infiltration event is able to saturate most of the random slope realizations regardless of the hydraulic properties. Inspection of developing F_s values with time during infiltration of the Kvam rainfall could clarify this. If the observation event included additional information on the time to failure or target pore pressure levels, more pronounced effect of updating may be expected for the hydraulic parameters.

As discussed in Section 2.2, infiltration in unsaturated slopes is a complex process in nature. The interaction between the involved variables; rainfall intensity, rainfall pattern, duration and hydraulic properties affect the developing pore pressures in both the numerical and analytical models. In this study, only one 24 h rainfall event is considered. Thus, the preceding discussions apply to this event. For better understanding of the effect of the infiltration process on landslide occurrence in the numerical and analytical models, updating with other rainfall events of varying rainfall intensities, patters and durations could be investigated. A wider range of k_{sat} could also be investigated. For this study, the selected coefficient of variation in k_{sat} (based on Melchiorre and Frattini (2012)) corresponds to no more variation than that typically observed in the shallow parts of till deposits. However, literature suggest that local variations in slopes can be of many orders of magnitude (Janbu (1970), Lars Lundin (1990b)).

The case study in this thesis alone is not sufficient to make general comments regarding the impact of model complexity on rainfall-induced landslide predictions. The large difference in number of realized samples between the two studies also complicates the comparison. As discussed in previous chapters, the analytical and numerical models have their advantages and disadvantages. The main argument for using analytical tools in Bayesian updating approaches is the generally low computational demands. No significant inconsistency between results of the different prediction tools is found in this study, in terms safety predictions, effects of updating or relative importance of controlling parameters.

4.5.3 (c) Future landslide predictions with analyical model

Results

In Figure 4.20 on the next page, the probability of failure, P_f, for 24 hour rainfall-events with different return periods are presented. The left figure 4.20 (a) shows probabilities calculated for present rainfall conditions, while failure probabilities in (b) are calculated for predicted worst case future conditions. The worst case scenario corresponds to an average increase of around 20% of present 24 hour rainfall amounts for all return periods (Ref. 4.8 page 52). The probabilities presented with solid lines are calculated with 20000 sample sets of the initial parameter distributions. Probabilities presented in dashed lines are calculated with 20000 sample sets of the posterior distributions after Bayesian updating is done in the analytical model.

Discussion

In Figures 4.20 (a) and (b), not surprisingly, the P_f estimates for all rainfall events are significantly lower when updated posterior distributions are used in calculation. The reductions are results of reduced uncertainties in the stability controlling parameters. The dashed lines in 4.20 show that increased rainfall intensities (due to higher return period or the climate change effect) make bigger differences in failure predictions after Bayesian updating.

The effect of increases in I_z on the estimated P_f is higher for low values of I_z. This observation can likely be associated with the effect of rainfall intensity on the slope response in the analytical model. For low intensity rainfalls, the slope may not be fully saturated in a 24 hour time frame in a large subset of the random realizations. As the I_z values become large, more of the slope realizations will become saturated and the rate of increase in P_f declines. P_f will only continue to increase with the rise in I_z until $I_z = k_s$ for the majority of the sample set realizations. This is because $I_z/k_s = 1$ defines the maximum infiltration rate in the analytical model (Ref. Section 2.2.4), and thus further increases should not make much difference in estimated stability conditions in the analytical model. As stated earlier, failure mechanisms due to rainwater and flooding erosion on the slope surfaces are not considered in the model.

Before updating, neither climate change nor increased return periods have significant effect on estimated failure probabilities. Thus, these results show that observations of slope survival can be utilized to increase the estimated safety of the slope and increase resolution in the slope reliability assessment.

An important observation is that the posterior P_f estimates are low for the highest θ values. This can again be attributed to the higher effectiveness of updating information for critical slopes. For steep slopes, the slope survival observations impose stronger constraints on the stability predictions and parameter distributions, because these slopes are generally more vulnerable to rainfall infiltration. Consequently, the uncertainties controlling occurrence of rainfall-induced landslides are reduced the most for these slopes. As assumed based on the effects of updating on the different parameters in Figure 4.14, stability is influenced the most by parameters c', H and H_w. When uncertainty in these critical parameters is reduced the most for high θ values, these updated slopes will be predicted more likely to survive future rainfalls. Thus, due to the effects

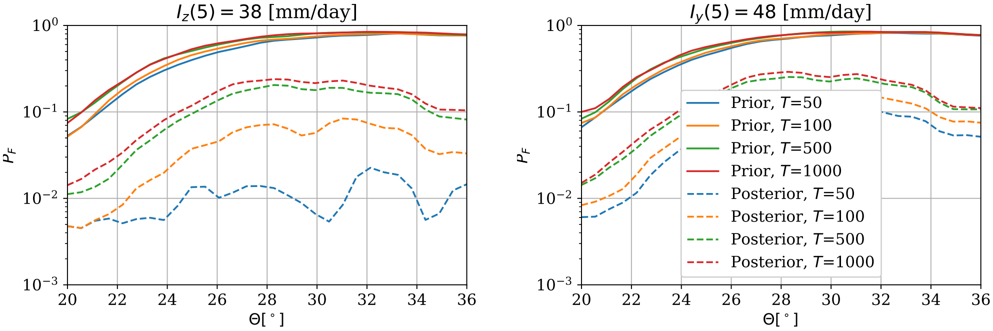

(a) **(b)**

Figure 4.20: *Prior and posterior estimates of slope failure probability for rainfall intensities [mm/day]: (a) Present scenario:* $I_z(T = 50)$*=59,* $I_z(T = 100)$*=68,* $I_z(T = 500)$*=93,* $I_z(T = 1000)$*=106. (b) Future worst case scenario:* $I_z(T = 50)$*=73,* $I_z(T = 100)$*=83,* $I_z(T = 500)$*=111,* $I_z(T = 1000)$*=125.*

of higher information strength, the posterior estimates of P_f display a decreasing trend for higher values of θ.

In b, the updated failure probabilities for the $T = 50$ return period rainfall under present conditions reveal some surprising results. The calculated 24 hour long rainfall intensity applied here is 59mm/day. The lowest dashed line represents failure probability for sample sets that are updated with the information of surviving a 24 hour rainfall of 60mm/day. Thus, one would expect that none of the slopes with the same sample sets would fail for a lower rainfall intensity. However, this is not the case in 4.20 (a), as the probability of failure for this T=50 rainfall events is higher than zero. This may be due to the modelling error, which is not reduced by updating. It is simply added to the prior and posterior estimates at the end of the calculation process, and failing slopes can thus be produced in the revaluation of stability.

The failure probability prediction for the $T = 50$ return period also illustrates how the variation in results will be high for small probabilities, due to insufficient number of failed slope sample sets. In order to increase accuracy in posterior estimates like this efficiently, subset simulation or similar techniques can be applied.

Lastly, the results of this climate change sub-study show that, in the implemented model, an 20% increase in five year rainfall intensity due to climate change only subtly decreases predicted stabilities. This is inferred from comparison of Figures 4.20 (a) and (b). The effect is least significant for the high return periods, as discussed. This analysis considered the estimated worst case future scenario. If other scenarios had been used, the climate effect would have been even less significant. In order to properly evaluate the effect of climate change on the analytical rainfall-induced landslide predictions, more thorough investigations are necessary. By taking into account variance in rainfall patters, durations and also other conditions affected by climate change like temperatures and snow-melting, the results may be different.

The focus of this contribution is to analyze the effect of including information of slope performance on the involved uncertainties and the stability predictions in the safety assessment of rainfall-induced landslides. Uncertainty in the modelling arises mainly from epistemic uncertainty on hydrological and geotechnical model parameters. It is shown that uncertainty in parameter value ranges is successfully reduced when the observation information event is constraining the outcome space of the random realizations. The probability distributions of the uncertain parameters that are critical in the definition of the updating information are shifted towards more likely ranges. These results demonstrate that Bayesian updating can be a helpful tool in reducing uncertainties in rainfall-induced landslide analysis. This provides a basis to develop more accurate landslide prediction models calibrated on local geotechnical and hydrological conditions.

The case study also illustrates an important advantage of doing probabilistic analyses compared to deterministic. In this probabilistic study, numerous combinations of parameters that are estimated to make up stable slopes in the Kvam area are revealed. Many aspects of probabilistic modelling that influences results has not been investigated in detail in this thesis. Christian (2004) demonstrated that the choice of probability distribution function can influence geotechnical reliability estimates a lot. Effects like this has not been investigated in this study. Furthermore, in order to get proper quantification and understanding of the propagation of uncertainties in the analysis, it would be necessary to carry out sensitivity analyses.

Chapter 5

Summary and Future Work

5.1 Summary and conclusions

This thesis examined the potential of implementing a Bayesian updating framework to reduce uncertainties in predictions of rainfall-induced landslides based on observations of slope performance. Two types of landslide prediction models for slope stability under rainfall infiltration were implemented: simple analytical models and sequentially coupled numerical models. The updating process was performed using direct Monte Carlo and subset simulation techniques. A case study based on landslide events that occurred in 2011 in the Kvam area in central Norway, was considered. The updating information and uncertain parameters of the prediction models were selected to reflect Kvam geotechnical and environmental conditions. The results indicated consistent trends between the analytical and numerical models in terms of updated posterior probability density functions.

The results showed that uncertainty in geotechnical and hydrological parameters controlling the occurrence of rainfall-induced landslides can be successfully reduced when the observation information in the updating process is constraining the outcome spaces of the random realizations. The updating most effectively reduced uncertainties in parameters that were the most critical in the definitions of slope performance in the prediction models. In the Kvam case study, these were: soil thickness, initial groundwater depth, cohesion and friction angle. The posterior distributions indicated that stable slopes were likely to be associated with higher friction angles and values of cohesion. An increasing rate of change between prior and posterior distributions was also observed for increasing slope angles. This result is due to the higher strength of the updating information on slopes that are more vulnerable to rainfall infiltration. For steep slope angles, lower values of slope thickness and initial groundwater levels were assigned higher posterior likelihoods.

The posterior distributions of the infiltration controlling parameters dry unit weight, void ratio, saturated coefficient of permeability and diffusivity were not significantly affected by the updating process. This result can be attributed to the definition of the slope survival observation; it was defined only by values of the slope safety factor before and after the rainfall event. The effects of the complex transient rainfall infiltration controlled by these parameters may not have been captured in neither the analytical nor numerical updating models.

The effects of updating on the predictive capacity of the analytical model under variable future rainfall intensities and return periods were evaluated. In general, the observation of a slope surviving a rainfall event lead to the reduction of probabilities of slope failure under future rainfall events. The strength of updating information and variations in rainfall return periods affected the estimated calculated occurrence probabilities. The results provide a basis to develop more accurate landslide prediction models calibrated on local geotechnical, hydrological and climate conditions.

5.2 Recommendations for Further Work

The Kvam case study models can be expanded to a regional model, incorporating slope angle data available in maps (NGI.no). A topography-based steady-state approach (Montgommery and Dietrich (1994), D'Odorico and Fagherazzi (2003), D' Odorico et al. (2005)) can then be used to estimate ground water conditions prior to rainfall events. Local observations of slope performance under historical Kvam rainfall events, as those provided by Schiliro and Cepeda (2016), can be used as updating information.

A more thorough investigation of Bayesian updating in the numerical prediction model is needed to properly evaluate the effect of model complexity in the updating process. This could involve running simulations for a larger range of slope angles. One could also evaluate the effects of updating on the predictive capacity of the numerical model under variable future rainfall intensities and return periods.

Lastly, implementation of local and global sensitivity analyses would assist in more accurate quantification of the uncertainties and understand the propagation of the uncertainties involved in the Kvam case study.

Bibliography

Anderson, S. A., Sitar, N., January 1995. Analysis of rainfall-induced debris flows. Journal of Geotechnical Engineering 121 (7), 544–552.

Au, S.-K., Beck, J. L., 2001. Estimation of small failure probabilities in high dimensions by subset simulation. Probabilistic Engineering Mechanics 16 (4), 263–277.

Baecher, G. B., Christian, J. T., 2003. Reliability and Statistics in Geotechnical Engineering. John Wiley Sons, Ltd.

Bishop, A. W., Alpan, I., Blight, G. E., Donald, I. B., 1960. Factors controlling the shear strenght of partly saturated cohesive soils, 503–532.

Brooks, R., 1964. Hydraulic properties of porous media. Hydrology papers 3.

Cao, Z., 2017. Probabilistic Approaches for Geotechnical Site Characterization and Slope Stability Analysis.

Cascini, L., Couomo, S., Pastor, M., G., S., 2010. Modelling of rainfall-induced shallow landslides of the flow-type. Journal of Geotechnical and Geoenvironmental Engineering 1, 85–98.

Cho, S. E., Lee, S. R., September 2002. Evaluation of surficial stability for homogeneous slopes considering rainfall characteristics. Journal of Geotechnical and Geoenvironmental Engineering 128 (9), 756–763.

Christian, J. T., October 2004. Geotechnical engineering reliability: How well do we know what we are doing? Journal of Geotechnical and Geoenvironmental Engineering 130 (10), 985–1003.

Collins, B. D., Znidarcic, D., April 2004. Stability analyses of rainfall induced landslides. Journal of Geotechnical and Geoenvironmental Engineering 130 (4), 362–372.

Conte, E., Troncone, A., March 2012. Simplified approach for the analysis of rainfall-induced shallow landslides. Journal of Geotechnical and Geoenvironmental Engineering 138 (3), 398–406.

D' Odorico, P., Fagherazzi, S., Rigon, R., March 2005. Potential for landsliding: Dependence on hyetograph characteristics. Journal of Geophysical Research: Earth Surface 110 (F1), n/a–n/a.

Darcy, H., 1856. Les fontaines publiques de la ville de dijon. Paris: Dalmot.

Depina, I., 2017. Learning about uncertain predictions of rainfall-induced landslides from observed slope performance. Internal report,Klima 2050 project.

division NTNU, G., 2015. Geotechnics Field and Laboratory Investigations, Lecture notes MSc Course TBA4110. Norwegian University of Science and Technology, Trondheim.

D'Odorico, P., Fagherazzi, S., 2003. A probabilistic model of rainfall-triggered shallow landslides in hollows: A long-term analysis. Water Resources Research 39 (9), n/a–n/a, 1262.
URL `http://dx.doi.org/10.1029/2002WR001595`

Duncan, J., Wright, S., 1980. The accuracy of equilibrium methods of slope stability analysis. Engineering Geology 16 (1), 5–17.

Edvardsen, D. H., 2013. Utløsningsårsaker og utløsningsmekanismer til flomskred i moreneavsetninger.

Ering, P., Babu, G. S., June 2016. Probabilistic back analysis of rainfall induced landslide- a case study of malin landslide, india. Engineering Geology 208, 154–164.

Fredlund, D. G., 2012. Unsaturated Soil Mechanics in Engineering Practice. Wiley, New York.

Fredlund, D. G., Morgenstern, N. R., Widger, R. A., August 1978. The shear strength of unsaturated soils. Canadian Geotechnical Journal 15 (3), 313–321.

Førland, E., Kristoffersen, D., 1989. Estimation of extreme precipitation in norway. Hydrology Research 20 (4-5), 257–276.

Galavi, V., 2010. Groundwater flow, fully coupled deformation and undrained analyses in plaxis 2d and 3d. Report published by Plaxis, retrived from s://www.plaxis.com/.

Griffiths, D. V., 2010. Stability analysis of slopes in variable soils by finite elements. Retrieved from `http://inside.mines.edu/~vgriffit/pubs/Some_C_Pubs/Minnesota_2010.pdf`.

Guan, Y., Fredlund, D. G., August 1997. Use of the tensile strength of water for the direct measurement of high soil suction. Canadian Geotechnical Journal 34 (4), 604–614.

Haldorsen, S., Krüger, J., 1990. Till genesis and hydrogeological properties. Nordic Hydrological Programme: Hydrogeological Properties of Nordic Tills (NHP report No 25), 3–26.

Heyerdahl, H., September 2016. Rainfall-induced landslides in quaternary soils in norway. E3S Web of Conferences 9.

Holm, G., 2012. Case study of rainfall induced debris flows in veikledalen.

Iverson, R. M., July 2000. Landslide triggering by rain infiltration. Water Resources Research 36 (7), 1897–1910.

Jaedicke, C., 2009. Økt skredfare kan avverges. KLIMA (1), 30–31.

Jaedicke, C., Solheim, A., Kronholm, L., Kristensen, K., Høydal, A., Blikra, A., Kronholm, K., Stalsberg, D., Sletten, K., Melchiorre, K., Vikhamar-Schuler, K., Isaksen, I., Sorteberg, C., Barstad, O., Aaheim, H., Mestl, H., July 2008. Spatial and temporal variations of norwegian geohazards in a changing climate, the geoextreme project. Natural Hazards and Earth System Science 8 (4), 893–904.

Janbu, N., 1970. Grunnlag i geoteknikk. Tapir.

Jørgensen, P., 1977. Some properties of norwegian tills. Boreas 6 (2), 149–157.

Lacasse, S., Nadim, F., 1997. Uncertainties in characterising soil properties. Publikasjon-Norges Geotekniske Institutt 201, 49–75.

Lars Lundin, Henrik Breuning Madsen, H. R., 1990a. Water movements in nordic till soils. Nordic Hydrological Programme: Hydrogeological Properties of Nordic Tills (NHP report No 25), 135–146.

Lars Lundin, Henrik Breuning Madsen, H. R., 1990b. Saturated hydrylauic conductivity of nordic tills. Nordic Hydrological Programme: Hydrogeological Properties of Nordic Tills (NHP report No 25), 67–74.

Lundin, L., 1982. Soil moisture and groundwater in till soil and the significance of soil type for runoff. UNGI Rapport No 56, 216 pp.

Luo, X., Liu, W., Fu, M., Huang, J., February 2017. Probabilistic analysis of soil-water characteristic curve with bayesian approach and its application on slope stability under rainfall via a difference equations approach. Journal of Difference Equations and Applications 23 (1-2), 322–333.

Melchiorre, C., Frattini, P., July 2012. Modelling probability of rainfall-induced shallow landslides in a changing climate, otta, central norway. Climatic Change 113 (2), 413–436.

Milledge, D. G., Griffiths, D. V., Lane, S. N., Warburton, J., September 2012. Limits on the validity of infinite length assumptions for modelling shallow landslides. Earth Surface Processes and Landforms 37 (11), 1158–1166.

Montgommery, D. R., Dietrich, W. E., April 1994. A physically based model for the topographic control on shallow landsliding. Water Resources Research 30 (4), 1153–1171.

Montrasio, L., 2000. Stability analysis of soil slip. Proceedings of International Conference "Risk 2000", 357–366.

NGI, 2013. Impacts of extreme weather events on infrastructure in Norway (InfraRisk) - Sluttrapport til NFR-prosjekt 200689. No. Authors: Frauenfelder, R., Solheim, A., Isaksen, K., Romstad, B., Dyrrdal, A.V., Gangstø, R., Harbitz, A., Harbitz, C.B., Haugen, J.E., Hygen, H.O., Haakenstad, H., Jaedicke, C., Jónsson, Á., Klæboe, R., Ludvigsen, J., Meyer, N.M., Rauken, R., Sverdrup-Thygeson, K., Aaheim, A. NGI report nr. 20091808-01-R. Norwegian Geotechnical Institute.

NGU, 2009. Resultater og anbefalinger fra geoextreme. `http://www.ngu.no/upload/Geofarer/Skred/GeoExtreme_folder.pdf`, accessed: 2017-12-12.

NGU, 2015. Norges Geologiske Undersøkelser geologisk ordliste. `https://www.ngu.no/side/geologisk-ordliste`, accessed: 2017-11-27.

NVE, e. N. v.-o., 2013. Faktaark: Jordskred og flomskred. Ansvarlig utgiver: Kjetil Hillestad.

of Petroleum, N. M., Energy, 2013. Climate change adaptation in Norway, Report Nr. 33 (2012-2013) to the Storting (white paper).

of the Environment, N. M., 2012. How to live with the dangers - flood and landslides, Report Nr. 15 (2011-2012) to the Storting (white paper). NB: only avaliable in Norweigan language.

Plaxis, 2016a. Plaxis 2d material models manual. Retrived from `https://www.plaxis.com/`.

Plaxis, 2016b. Plaxis 2d refrence manual. Retrived from `https://www.plaxis.com/`.

Plaxis, 2016c. Splaxis 2d scientific manual. Retrived from `https://www.plaxis.com/`.

Rahardjo, H., O. T. R. R., Leong, E., December 2007. Factors controlling instability of homogeneous soil slopes under rainfall. Journal of Geotechnical and Geoenvironmental Engineering 133 (12), 1532–1543.

Richards, L. A., November 1931. Capillary conduction of liquids through porous mediums. Physics 1 (5), 318–333.

Sandersen, F., Bakkehøi, S., Hestnes, E., Lied, K., 1996. The inuence of meteorological factors on the initiation of debris ows, rockfalls, rockslides and rock mass stability, 97–114.

Schiliro, L., Cepeda, J., 2016. Physically-based modelling of landslides in Kvam (Nord-Fron commune) triggered on 9-10 June 2011. No. 2016-08-12 DRAFT in 20150145-01-05-R. Norwegian Geotechnical Institute.

Schilirò, L., Montrasio, L., Scarascia Mugnozza, G., November 2016. Prediction of shallow landslide occurrence: Validation of a physically-based approach through a real case study. Science of the Total Environment 569-570, 134–144.

Straub, D., Papaioannou, I., March 2015. Bayesian updating with structural reliability methods. Journal of Engineering Mechanics 141 (3).

Tsai, T.-L., Yang, J.-C., Jul 2006. Modeling of rainfall-triggered shallow landslide. Environmental Geology 50 (4), 525–534.
URL `https://doi.org/10.1007/s00254-006-0229-x`

Van Genuchten, M., 09 1980. A closed-form equation for predicting the hydraulic conductivity of unsaturated soils1. Soil Science Society of America Journal 44.

Vogel, T., van Genuchten, M., Cislerova, M., 2000. Effect of the shape of the soil hydraulic functions near saturation on variably-saturated flow predictions. Advances in Water Resources 24 (2), 133–144.

Walberg, N. A. K., Devoli, G., 2014. Regional varsling avjordskredfare: Analyse av historiske jordskred, flomskred og sørpeskred i Gudbrandsdalen og Ottadalen. No. nr. 44 - 2014 in Rapport. Norges vassdrags- og energidirektoratet.

Wang, Y., Cao, Z., Au, S.-K., January 2011. Practical reliability analysis of slope stability by advanced monte carlo simulations in a spreadsheet. Canadian Geotechnical Journal 48 (1), 162–172.

Wasserman, L., 2006. All of nonparametric statistics.

Zhan, T. L. T., Jia, G. W., Chen, Y., Fredlund, D. G., Li, H., August 2013. An analytical solution for rainfall infiltration into an unsaturated infinite slope and its application to slope stability analysis. International Journal for Numerical and Analytical Methods in Geomechanics 37 (12), 1737–1760.

Zhang, J., Tang, W. H., Zhang, L. M., January 2010. Efficient probabilistic back-analysis of slope stability model parameters. Journal of Geotechnical and Geoenvironmental Engineering 136 (1), 99–109.

Zhang, L., Li, J., Li, X., Zhang, J., Zhu, H., June 2016. Rainfall-Induced Soil Slope Failure, 1st Edition. CRC Press.

Zhang, L. L., Zhang, J., Zhang, L. M., Tang, W. H., 2011. Stability analysis of rainfall-induced slope failure: a review. Proceedings of the ICE - Geotechnical Engineering 164 (5), 299–316.